University of Padova
Department of Information Engineering

ICT for Internet & Multimedia
Master Thesis

Quantitative assessment of structural connectivity alteration in glioma patients through diffusion kurtosis imaging and graph metrics

Supervisor:
Alessandra Bertoldo

Assistant supervisor:
Maria Colpo

Author:
Francesco Guarnaccia

ID: 1234378

A MIA MADRE, MIO PADRE, MIO FRATELLO

E TUTTI COLORO CHE, STANDOMI ACCANTO, SONO DIVENTATI ABILI CONOSCITORI DELL'ARTE, A ME PREZIOSA, DI ESSERE BENEFATTORI PER IL MIO EQUILIBRIO INTERIORE.

Abstract

Diffusion Kurtosis Imaging (DKI) is a Neuroimaging analysis technique that models the water molecules diffusion pattern and shapes the complex brain microstructural environment through the extraction of specific diffusion metrics. This kind of methodology has proved to be an alternative and effective inspection tool especially in pathologic applications, such as de novo gliomas. Glioma, defined as a brain tumour originating in the supportive glial cells, has an infiltrative behaviour in the white matter brain tissue, potentially leading to the disruption or displacement of the axonal fibers. In this context, DKI was exploited to assess the glioma grade, to differentiate glioma recurrence from pseudo-progression and to investigate the proliferative activity of cancer cells. In addition, DKI revealed to be a powerful tool to also evaluate the alteration of the microstructure environment at the centre and periphery of the glioma lesion. The work of this thesis includes both the application and evaluation of a neural-networks optimization-based non-linear estimation algorithm used to fit the DKI model, followed by the diffusion metrics extraction, and the employment of graph techniques to associate the diffusion metrics with the brain diffusion microstructural connectivity evaluation. The final result of this project is to provide a quantitative analysis of brain microstructure parameters in patients affected by glioma, including the extraction of graph measures thought to be associated with functional activation patterns. The main aim of this project is to identify a preferred functional activation pattern based on diffusion microstructure parameters region-specific correlation through graph theory assessment methodology.

Contents

Chapter 1

Introduction

1.1 Gliomas and Diffusion Weighted Imaging.

1.1.1 Gliomas general introduction

Gliomas are the most frequent primary tumors of the central nervous system (CNS) and form a heterogeneous group of neoplasms with multiple histologic types and malignancy grades. Gliomas are considered to originate from glial cells or stem cells that develop glial characteristics upon neoplastic transformation. The term glioma includes astrocytic tumors, oligodendrogliomas, ependymomas, and mixed gliomas. The vast majority of glial neoplasms in adult patients are diffuse gliomas. Such gliomas are characterized by diffusely infiltrative growth within the CNS parenchyma, with tumor cells invading individually or as groups of cells forming a network throughout the neuropil. Diffuse glioma growth is often further accompanied by aggregation of neoplastic cells around neurons and blood vessels. Moreover, diffuse gliomas tend to invade over large distances along myelinated fiber tracts, quite frequently crossing the corpus callosum into the opposite hemisphere, generating the so-called 'butterfly glioma' pattern [1].

Histopathologically, the tumor cells have the tendency of pervading individually or in small groups in between the dense network of neuronal and glial cell processes. In large areas of diffuse gliomas, the tumor cells exploit pre-existent "supply lines" for oxygen and nutrients rather than constructing their own [2].

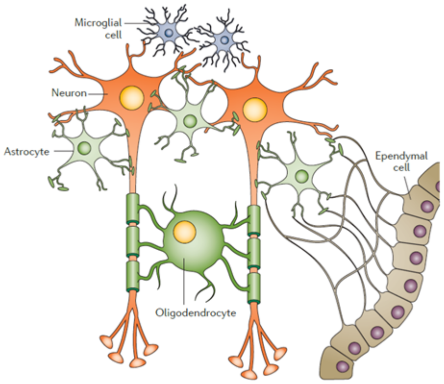

Figure 1.1: Types of brain cells [2].

Until recently, the histologic diagnosis was the main reference for the classification, conveying important prognostic information and forming the basis for further patient management. However, classification of gliomas can be challenging because of inadequate tissue sampling, imprecise diagnostic criteria, and because the biology of gliomas is not fully represented by its histology alone [3].

Magnetic Resonance Imaging (MRI) is now the gold standard for defining brain tumor anatomy in a clinical setting. Challenges for imaging include not only the diagnos¬tic accuracy for unknown lesions but also the sensitivity and, even more importantly, the specificity of follow up images in the context of therapy-induced changes, termed pseudoresponse and pseudoprogression. Conventional MRI sequences commonly used for evaluation of intracranial malignancy include T1-weighted (T1W), T2-weighted (T2W), fluid attenuated inversion recovery (FLAIR), T2*W gradient echo and post-contrast T1W images. These sequences provide sharp anatomic details, and the use of a gadolinium-based contrast agent in this protocol allows for the detection of areas where the blood-brain barrier is compromised [4].

Clinically, gadolinium-enhanced MRI is considered the primary imaging modality for initial work up and follow up of patients with gliomas, although it has some limitations, especially in differentiating high from low grade tumours and in distinguishing disease recurrence from post-therapy changes. Hybrid positron emission tomography (PET)/MRI is a relatively novel tool that combines MRI sequences with metabolic information from PET in a single scan [5].

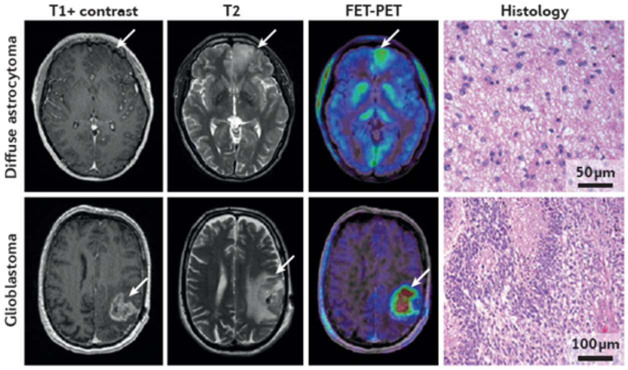

Figure 1.2: Neuroimaging and histological features of gliomas [2].

Thanks to these different techniques, gliomas can be classified from a histological perspective, by disease severity grade and by spreading location. Histologically, gliomas are named according to the specific cell with which they share most of their cytological features, but not necessarily from which they originate [2]. The main types of gliomas are:

- Ependymomas: ependymal cells.
- Astrocytomas: astrocytes.
- Oligodendrogliomas: oligodendrocytes.
- Brainstem gliomas: develop in the brain stem.
- Optical nerve gliomas: originate in or around the optical nerve.
- Mixed gliomas: includes cell of different types of glia.

Gliomas are further categorized according to their grade, which is determined by pathologic evaluation of the tumour. The neuropathological evaluation and diagnostics of brain tumour specimens is performed according to the World Health Organization (WHO) Classification of Tumours of the Central Nervous System. The WHO glioma grading has the following composition:

- **Grade I**: gliomas are slow growing, usually well-demarcated and are associated with favourable prognoses.
- **Grade II**: gliomas are also slow growing but often show brain-invasive growth that precludes complete resection.
- **Grade III**: gliomas are rapidly growing high-grade tumours characterized by histological features of anaplasia, in particular high cellularity, cellular pleomorphism, increased nuclear atypia and brisk mitotic activity.

- **Grade IV**: is reserved for glioblastomas, variants include giant cell glioblastoma and gliosarcoma. Glioblastomas are the most malignant gliomas that are microscopically distinguished from WHO grade III anaplastic astrocytomas by the presence of pathological microvascular proliferation and areas of necrosis. [2]

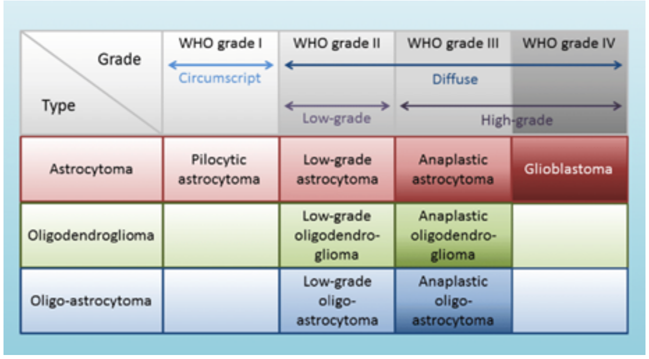

Grade Type	WHO grade I	WHO grade II	WHO grade III	WHO grade IV
	Circumscript	Diffuse		
		Low-grade	High-grade	
Astrocytoma	Pilocytic astrocytoma	Low-grade astrocytoma	Anaplastic astrocytoma	Glioblastoma
Oligodendroglioma		Low-grade oligodendro-glioma	Anaplastic oligodendro-glioma	
Oligo-astrocytoma		Low-grade oligo-astrocytoma	Anaplastic oligo-astrocytoma	

Figure 1.3: Classification of glioma in types and WHO grades [6].

More recently, as the use of molecular biomarkers in brain and spinal cord tumor diagnosis has been further elucidated, challenges have arisen in how to organize the classification of tumor types. Some are readily and consistently characterized by defining molecular features; for some, molecular parameters are not required but may support their classification; yet others are rarely or never diagnosed using molecular approaches. The resulting organization is therefore also mixed. For this reasons the WHO has introduced a more detailed and specific classification of tumors of the central nervous system [7]. This fifth edition of tumor classification, called WHO CNS5, has grouped tumors according to the genetic changes that enable a complete diagnosis, such as isocitrate dehydrogenase (IDH) muation, by looser oncogenic associations, by histological and histogenetic similarities, even though molecular signatures vary, and by using molecular features to define new types and subtypes. This hybrid taxonomy represents the current state of the field but is likely only an intermediate stage to an even more precise future classification [7]. In particular, the main types of gliomas, glioneuronal tumors and neuronal tumors are divided as follows:

- Adult-type diffuse gliomas: Astrocytoma, Oligodendroglioma and Glioblastoma.
- Pediatric-type diffuse low-grade gliomas: Diffuse astrocytoma, Angiocentric glioma and Diffuse low-grade glioma.
- Pediatric-type diffuse high-grade gliomas: Diffuse midline glioma, Diffuse hemispheric glioma, Diffuse pediatric-type high-grade glioma and Infant-type hemispheric glioma.

- Circumscribed astrocytic gliomas: Pilocytic astrocytoma, High-grade astrocytoma with piloid features, Subependymal giant cell astrocytoma, Chordoid glioma and Astroblastoma.
- Glioneuronal and neuronal tumors: Ganglioglioma, Papillary glioneuronal tumor, Myxoid glioneuronal tumor, Gangliocytoma, Central neurocytoma and Extraventricular neurocytoma.
- Ependymal tumors: Supratentorial ependymoma, Spinal ependymoma, Posterior fossa ependymoma, Myxopapillary ependymoma and Subependymoma.
- Embryonal tumors: molecular-defined Medulloblastomas and histological-defined Medulloblastomas.

Finally, gliomas can be classified according to whether they are above or below a membrane in the brain called the tentorium, which separates the cerebrum (above) from the cerebellum (below).

It is fundamental to highlight that, of all above mentioned classification methods, the one of the WHO is the most exploited in order to provide diagnosis, prognosis and to assess possible treatment approaches [8]. Despite its widespread use, the WHO histopathological classification is limited by substantial interobserver variability and poor correlation with clinical outcome [9].

The recognition of diffuse infiltrative versus other types of glial tumors has significant prognostic and therapeutic implications. While the diffuse infiltrative growth pattern is characteristic for both low- and high-grade diffuse gliomas, the exact growing scheme of gliomas cannot always be assessed in biopsy specimens, but specific histopathological features strongly favor a diffuse infiltrative nature of the glial neoplasm. Glioma cells can disseminate via white matter tracts, cerebrospinal fluid pathways, or meninges and thus give rise to multifocal gliomas. In addition, compared to low-grade diffuse gliomas, high-grade tumors are often radiologically more heterogeneous and are accompanied by more severe edema. The occurrence of contrast-enhancement in diffuse gliomas generally signifies a more malignant biological behavior. Furthermore, it is important to realize that the diffuse infiltrative growth pattern is not just the result of malignant progression as both low- and high-grade diffuse gliomas display this phenomenon. Therefore, in a clinical setting combination of clinical, radiological, and pathological information is warranted to avoid diagnostic inaccuracy, particularly in cases where only small biopsy specimens are available for histopathological diagnosis [10].

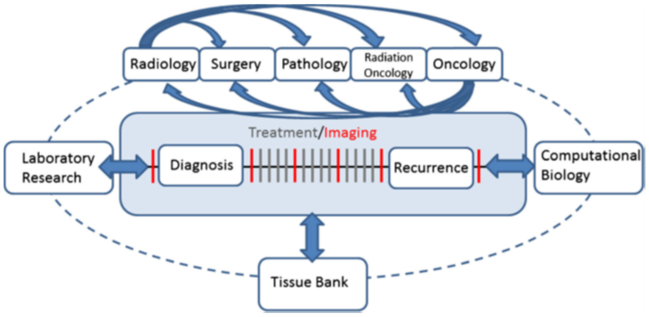

Figure 1.4: Multidisciplinary approach to treatment of glioma [11].

1.1.2 Diffusion Weighted Imaging (DWI) for glioma applications

New MR modalities may contribute to better radiological classification and delineation of glial brain tumors as well as assist in identification of the best spot for a biopsy. With the development of diffusion-weighted MR pulse sequences in which strong diffusion gradients are used, images can be obtained that are dependent on the diffusion of water molecules. These images reflect the molecular translational motion, Brownian motion, of water within the section of interest. DWI, along with a related approach called diffusion tensor imaging (DTI), can thus be used to image indirectly infiltration of glioma cells in normal brain tissue.

From a few decades, DWI has started to be employed in clinical applications in order to provide additional neuroimaging information for the pathological evaluation of the lesion. In fact, Tien et al. conducted one of the first innovative works with the purpose of evaluating the usefulness of diffusion weighted echoplanar MR imaging in the examination of high-grade brain gliomas compared with that of conventional spin-echo (SE) or fast spin-echo (FSE) MR imaging. After the examination of the diffusion weighted images, in particular of the apparent diffusion coefficient (ADC) map, they concluded that DWI is a useful technique for investigating high-grade cerebral gliomas, enabling the differentiation of various components of the tumor and the distinguishment of areas of predominantly non-enhancing tumor from areas of predominantly peritumoral edema [12].

A few years later, Sugahara et al. published a study to assess the utility of diffusion MRI, with echo-planar imaging (EPI) technique, in depicting the tumor cellularity and grading of gliomas. Their main findings regard the higher sensitivity of the ADC map compared to the anatomical sequences. In fact, tumor cellularity correlated well with the minimum ADC value of the gliomas, but not with the signal intensity on the T2-weighted images. In addition, the minimum ADC of the high-grade gliomas was significantly higher than that of the low-grade gliomas. These results led to the conclusion that this combination of imaging approaches reveals crucial information that cannot be obtained with standard MRI acquisition sequences [13].

More recently, the research activity has been focused on analyzing the role of Diffusion-weighted MRI as a biomarker for treatment response in glioma. Since ADC is inversely correlated with tumor cell density, this measure can be used for detecting probable invading tumor cells that are not always visible with the anatomical images. In addition, functional diffusion maps (fDMs) approach, which shows ADC changes over time, exhibited a promising marker of response to chemotherapy within enhancing lesions. The final results of this findings expressed the fDMs potential to predict response to newer therapeutic regimens earlier than standard radiologic assessment criteria [14].

A peculiar diffusion weighted model, called Perfusion imaging, is able to capture the tumor abnormal microvascular environment, allowing a better understanding of the tumour biology and vasculature. In this context, MR perfusion imaging provides information potentially relevant to tumour grade, treatment response and tumour aggressiveness. Perfusion imaging is in widespread use clinically, and it has been shown to prospectively impact the confidence of both imagers in assessing tumour status and clinicians in determining treatment plans [15].

With the advancing technology and methodology, DWI now relies on more complex reconstruction models in order to extract diverse type of information from the acquired images. Exploiting these computational means, Bai et al. focused on studying how combined model-fitting strategies can be helpful for the assessment of glioma grade. In particular, given that the DWI is an exponential decaying signal, they compared the potential of various diffusion parameters obtained from monoexponential, biexponential, and stretched exponential diffusion-weighted imaging models and diffusion kurtosis imaging. This integrated procedure led to the conclusion that different diffusion metrics may provide additional information and improve the grading of gliomas compared with conventional diffusion parameters [16].

More recently, histogram ADC maps profiling has been proved to be a valuable biomarker both in low-grade (LGGs) and high-grade gliomas (HGGs). Starting from low grade gliomas, Gihr et al. provided an in vivo characterization of tumor architecture and corresponding neuropathology. Specifically, they investigated whether histogram profiling of ADC distinguishes grade I from grade II glioma, reflects the proliferation index Ki-67 and associates with molecular characteristics, such as isocitrate dehydrogenase (IDH) mutation. Their findings revealed that ADC histogram-profiling is a valuable radiomic approach, which helps differentiating tumor grade, estimating growth kinetics and probably prognostic relevant genetic alterations in LGGs [17].

Soon after, the same research team led by Gihr, applied the same analysis approach to high grade glioma. In addition, they included the correlation with the prognostic relevant MGMT (methylguanine- DNA methyltransferase) promotor methylation status. The outcomes of this retrospective study showed that ADC histogram parameters differ significantly between glioblastoma and anaplastic astrocytoma and exhibit distinct associations with the proliferative activity in both HGG, suggesting that ADC histogram profiling as promising biomarker for differentiation of both types of high-grade gliomas [18].

Future works are moving to the improvement of noninvasive classification of glioma genetic subtype with deep learning and diffusion weighted imaging. In this scenario, convolutional neural networks are trained in order to provide the genetic subtype classification receiving as input the acquired diffusion weighted images. The results not only confirm the significant support of the artificial intelligence, exploiting in particular transfer learning strategies, in clinical applications, achieving classification accuracies above 85% [19].

1.2 Diffusion Tensor Imaging and Diffusion Kurtosis Imaging

1.2.1 Diffusion Tensor Imaging (DTI) model

The human brain anatomical composition is made by three main different types of tissues, corresponding to the different kind of cells and structures inside it. Starting from the neurons, they are particular cells belonging to the brain tissue that are composed by a body, which contains the nucleus and the cytoplasm, and some extensions of this body that are distinguished in dendrites and axons. The two main differences between these two kinds of structures are that dendrites are much shorter than axons and are employed by the neuron for information integration, while axons, being significantly longer, are principally devoted to information communication and are covered with a myelin sheath. Therefore, axons are the principal communication ways for establishing connections among neurons, which are mainly designated to carry out information processing. It is important to highlight the fact that the term information refers to, anatomically and physiologically speaking, electrical and chemical stimuli. In addition, glial cells, useful for support, nutrition and protection of the neurons, are to be considered in the whole composition of the brain tissue, along with the cerebrospinal fluid and the blood vessels. Usually, neurons are referred to as Grey Matter(GM), while axons and dendrites as White Matter(WM) [20].

In this complex assemble of different anatomic structures, Diffusion Tensor Imaging (DTI) techniques is able to capture the principal directions of diffusion of water molecules that can be facilitated or hindered by all the microstructures belonging to the brain tissue. Before going into the details of the diffusion topic, it may be useful to introduce the basic concepts of Magnetic Resonance Imaging (MRI) working principle and the corresponding signal acquired. This particular technique relies on the “spin” property of the atomic nucleus of certain elements, such as hydrogen H or phosphorus P, that can be interpreted as the nucleus spinning around its own axis, generating a local magnetic field. More specifically, to each atomic nucleus is associated a spin characterized by its own spin momentum M, by a spin number N and 2N + 1 energy levels. If the number of protons and neutrons in the atom is not the same, it results that N0 and it is therefore possible to define a magnetic momentum defined as =N in which stands for the gyromagnetic ratio. In absence of external magnetic fields, the magnetic moments of the various spin have random directions whose resultant is zero. However, the application of an external magnetic field B0 with high intensity, always present and constant along a direction (usually the z direction in the scanners), causes the orientation of the magnetic moments of the spin along the direction of B0. The application of other non-constant external fields, called gradients, in the various directions of space causes the local alteration of the field B0 and allows to derive important parameters, such as the relaxation times T1 and T2, which are related to the spin and characteristic of the tissue to which they belong [21].

Once described the basic working principle of the MRI signal, it is now important to explain the concept of diffusion in order to later introduce the Diffusion MRI (dMRI) acquisition technique. Physically, diffusion is defined as the thermal translation movement of water molecules. Within this phenomenon, two different types of movement can be distinguished: one refers to an isotropic diffusion of molecules, meaning that there is not a preferential direction of diffusion, and the other regards an anisotropic dynamic of the movement of particles, in which instead a privileged diffusion trajectory can be detected. Considering the first diffusion condition mentioned, in order to mathematically describe the process, is fundamental to introduce the diffusion coefficient D, that is calculated according to the formulation derived from the Stokes-Einstein relation:

$$\mathrm{D{=}kT}/6\pi\eta\mathrm{r}$$

in which k is the Boltzmann constant, T is the temperature measured in Kelvin, η stands for the viscosity of the fluid considered and r indicates the radius of the molecules.

With this kind of definition, the expansion of the diffusion kinetics is assumed to be equal in every direction. Regarding the anisotropic diffusion instead, the calculation of the only D value is no longer sufficient to quantify the diffusion extent in different directions, so the specification of the Diffusion Tensor (DT) is needed in order to consider a more suitable and reliable formulation for this kind of dynamic. The DT describes the diffusion of water molecules using a Gaussian Model and is defined as a 3x3 matrix that reads:

$$\mathrm{DT}{=}\begin{bmatrix} D_{xx} & D_{xy} & D_{xz} \\ D_{yz} & D_{yy} & D_{yz} \\ D_{zx} & D_{zy} & D_{zz} \end{bmatrix}$$

and represents the mathematical model used to perform subsequent analysis in Diffusion Tensor Imaging analysis [22].

DTI consists in an established and reliable MRI technique for imaging the diffusion of water molecules in human tissues, particularly useful for visualizing white matter structures in the brain. This MRI acquiring strategy is based on the Steijskal-Tanner acquisition sequence, which is specifically designed in order to relate the dMRI output signal with the diffusion of water molecules in different directions. This kind of implementation allows to describe the extent of water diffusion with a rotationally invariant description, consequently enabling the characterization of complex white matter tracts. The renowned specific Steijskal-Tanner sequence is composed by two oscillating radio frequency (RF) pulses, respectively at 90° and 180° (degrees), both with equal intensity but opposite direction and separated in time by the interval $\frac{T_E}{2}$, which is exactly corresponding to the half echo time of the acquisition sequence. In addition to this RF pulses, gradient pulses of intensity G and lasting period δ are inserted symmetrically beside the 180° RF pulse, in terms of timing interval, separated by a time gap . These additional gradients play a crucial role in order to build echo-planar sequences that allow a reduction of the artifacts present during the scanning session, such as cardiac and CSF pulsations, and movement. Given that the effect of the gradient pulses is strictly related to the position, if the spins are subjected to motion, they will experience a phase shift, resulting in a significant reduction of the total magnetization. Diffusion imaging works by introducing extra gradient pulses whose effect discards the stationary water molecules and causes a random phase shift for molecules that diffuse.

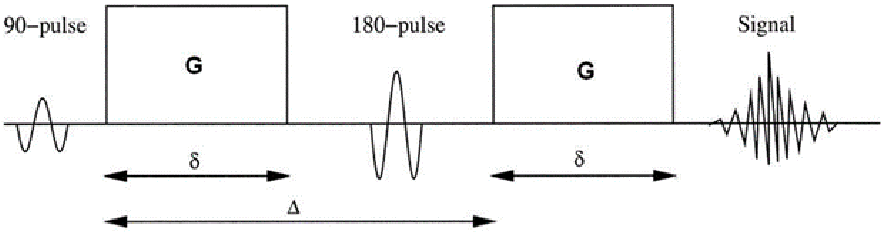

Figure 1.5: Stejskal-Tanner acquisition sequence [23]

In addition, the b-value allows to calculate both the Apparent Diffusion Coefficient(ADC), in case of isotropic diffusion, and the Diffusion Tensor for anisotropic diffusion. Starting from the first dispersion condition, the ADC computation is expressed as:

$$ln\left(\frac{S}{S_0}\right) = -ADC \cdot b$$

Concerning the diffusion tensor instead, it describes the diffusion of water molecules using a Gaussian Model that models the displacements of the molecules. The DT consists in a symmetric and positive-definite matrix, with 3 orthogonal eigenvectors and three positive eigenvalues. The major eigenvector of the diffusion tensor points in the principal diffusion direction that corresponds to the direction of the fastest diffusion. In anisotropic fibrous tissues the major eigenvector also defines the fibre tract axis of the tissue, and thus the three orthogonal eigenvectors can be thought of as a local fibre coordinate system. The three positive eigenvalues, $\lambda_1, \lambda_2,\ \lambda_3$, of the tensor give the diffusivity in the direction of each eigenvector. . Together, the eigenvectors and eigenvalues define an ellipsoid that represents an iso-surface of diffusion probability. In order to have a more reliable and useful interpretation of the diffusion tensor, the eigenvalues are used to provide a suitable computation of some diffusion metrics that allow to understand the water propagation distribution [24].

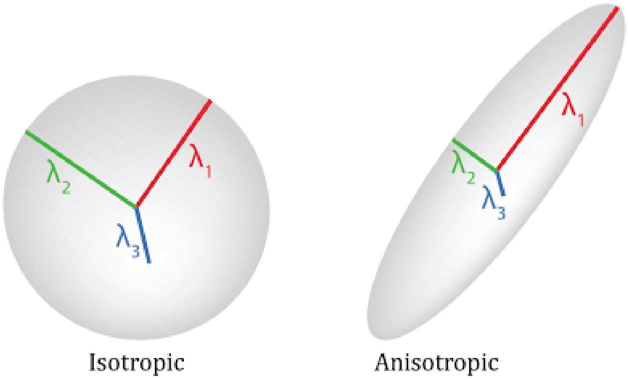

Figure 1.6: Ellipsoid mathematical model [24].

To obtain an overall evaluation of the diffusion in a voxel or region, it is crucial to consider an invariant factor that is independent of the orientation. In this case the invariant component of the diffusion tensor corresponds to its trace, defined as:

$$Tr\left(DT\right) = D_{xx} + D_{yy} + D_{zz}$$

and it is useful for the calculation of the Mean Diffusivity (MD) parameter, expressed as:

$$MD = \frac{Tr(DT)}{3}$$

Another useful parameter is the Apparent Diffusion Coefficient (ADC) that represents the magnitude of diffusion of water molecules within tissue, calculated as the mean of the three eigenvalues of the diffusion tensor matrix:

$$ADC = \frac{\lambda_1+\lambda_2+\lambda_3}{3}$$

On the other hand, tensor anisotropy is measured by ratios of the eigenvalues used to quantify the shape of the diffusion and the amount of tissue organization. The main measures used in order to extract some useful information from DTI images are: Fractional Anisotropy, Axial Diffusivity, Radial Diffusivity and Volume Ratio. It is crucial to highlight that the following metrics formulations are not fixed but may differ in some values combination, however without altering the semantic of the parameters. The fractional anisotropy, or FA, is the most widely used anisotropy measure, and, as the name suggests, it measures the fraction of the diffusion that is anisotropic. The FA parameter can be interpreted as the difference of the tensor ellipsoid with the sphere shape, calculated as a normalized variance of eigenvalues:

$$FA = \frac{1}{\sqrt{2}} \frac{\sqrt{(\lambda_1-\lambda_m)^2+(\lambda_2-\lambda_m)^2+(\lambda_3-\lambda_m)^2}}{\sqrt{\lambda_1+\lambda_2+\lambda_3}}$$

in which λ_m is referring to the mean value of the eigenvalues. FA is often considered a measure of white matter integrity, but it is important to underline that changes in the FA value may be caused by several different factors. The Axial Diffusivity (AD) refers to the magnitude of diffusion parallel to fiber tracts. Mathematically, the AD measure corresponds to the major eigenvector, λ_1, of the diffusion tensor, and the lowering of AD might reflect axonal injury, reduced axonal radius or less coherent orientation of axons. Moving forward, Radial Anisotropy (RA) gives information on the ratio between the isotropic and anisotropic components of the diffusion tensor. In particular, RA is defined as:

$$RA = \frac{1}{\sqrt{3}} \frac{\sqrt{(\lambda_1-\lambda_m)^2+(\lambda_2-\lambda_m)^2+(\lambda_3-\lambda_m)^2}}{\lambda_m}$$

Finally, the Volume Ratio (VR) takes into consideration the ratio between the volume of the ellipsoid and the one of a perfect sphere of radius λ_m, and it is expressed as:

$$VR = \frac{\lambda_1 \cdot \lambda_2 \cdot \lambda_3}{{\lambda_m}^3}$$

From these metrics it is possible to create maps of values, ranging from 0 to 1, which allow to evaluate not only the dynamics and extent of water diffusion within the brain microstructures, but also the white matter structural integrity [22].

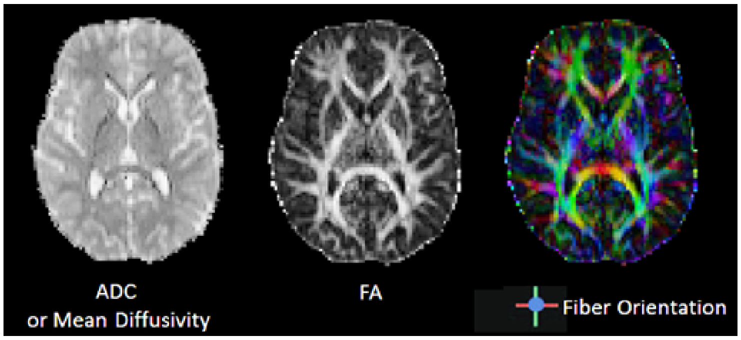

Figure 1.7: Maps derived from the diffusion metrics [22].

1.2.2 Diffusion Kurtosis Imaging (DKI) model

An extension of the DTI model is the so-called Diffusion Kurtosis Imaging, which takes into consideration the kurtosis contribution to the diffusion processes. Since the DTI formulation assumes that the water molecules displacement function is Gaussian shaped, it is necessary to introduce an additional measure in order to assess the extent of the non-Gaussian properties of the diffusion dynamics. In fact, in the complex brain tissue composition and with high b-value acquisition protocols, the Gaussian model leaks of precision while assessing the diffusion metrics, leading to the need of computing an additional measure. The latter consists in the kurtosis, which by mathematical definition corresponds to the quantification of the deviation of a probability density function (PDF) of interest from the Normal PDF, for which the kurtosis in equal to zero. In particular, if the PDF if more peaked than a Gaussian with shorter tails the kurtosis index is grater than 0, otherwise is lower than zero [25].

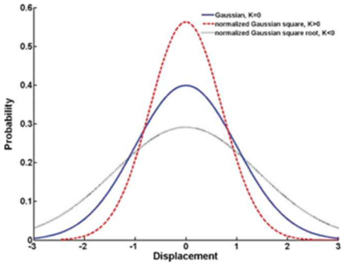

Figure 1.8: Kurtosis analytical definition [25]

In the context of the dMRI signal, the deviation from the Gaussian behaviour is significantly influenced by the degree of tissue complexity, thus the excess kurtosis can provide a reliable index to evaluate the proportion of organized microstructures within the water molecules diffuse. Being an extension of the DTI model, the DKI acquisition sequence still refers to the one of Stejskal-Tanner used for DTI, with the only difference that the b-values for the kurtosis estimation need to be larger compared to the ones used for DTI, specifically above 1000 but not greater than 3000 $\frac{mm}{s^2}$. DKI also offers a better fit to the diffusion data acquired with b-value above 1000 $\frac{mm}{s^2}$, since the kurtosis term contributes to the deviation of the model fitting curve, resulting in an improved goodness of fit. It is fundamental to underline that the DKI framework is a model independent approach that describes the diffusion weighted signal without imposing any biophysical assumption. Finally, DKI provides a practical clinical technique for quantifying non-Gaussian water diffusion and for probing the microscopic structure of biologic tissues [26].

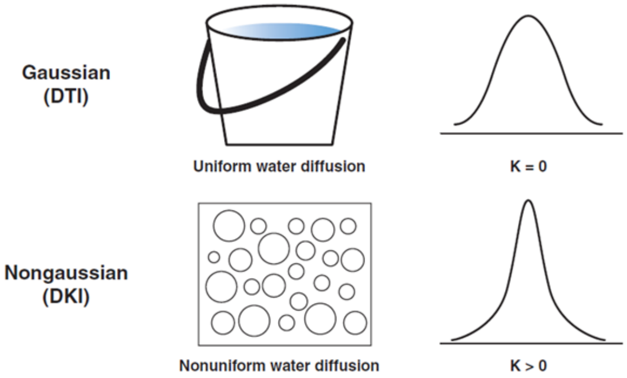

Figure 1.9: DTI vs DKI diffusion displacement model [27].

The analytical model of the DKI, as mentioned before, consists in the Taylor expansion of the logarithm formulation of DTI, resulting in:

$$\ln\left[S\left(b\right)\right] = \ln\left[S\left(0\right)\right] - bD_{app} + \frac{1}{6}b^2D_{app}^2K_{app}$$

in which D_{app} and K_{app} represent the apparent diffusion and kurtosis coefficients respectively. Knowing that D_{app} is an estimate of the diffusion coefficient in the orientation parallel to the diffusion sensitizing gradients, K_{app} corresponds to the index of diffusional kurtosis along the same direction.

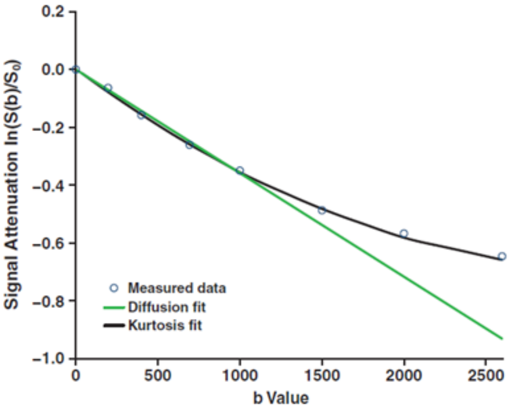

Figure 1.10: DTI vs DKI model fit [27].

In general, the measured diffusional kurtosis depends on the direction of the diffusion sensitizing gradients. This dependence on direction is described by a tensor with 15 independent components. As for the DT, in order to determine the full diffusional kurtosis tensor, the diffusional kurtosis must be measured in at least 15 different directions. Analytically, the tensor is defined as:

$$W_{ijkl}\left(t\right) = 9 \cdot \frac{<s_i s_j s_k s_l> - <s_i s_j><s_k s_l> - <s_i s_k><s_j s_l> - <s_i s_l><s_j s_k>}{<\mathbf{s} \cdot \mathbf{s}>^2}$$

where s_i indicates a directional component of the displacement vector $\mathbf{s}$ [26]. Therefore, it is possible to introduce the formulation of the diffusional kurtosis coefficient, nominally K_{app}, along an arbitrary direction, that reads:

$$K_{app} = \frac{MD^2}{D_{app}^2} \cdot \sum_{i=1}^{3} \sum_{j=1}^{3} \sum_{k=1}^{3} \sum_{l=1}^{3} n_i n_j n_k n_l W_{ijkl}$$

in which n_i represents the i-th element of the diffusion direction [25].

It is important to highlight the fact that the K_{app} is much more sensitive, compared to the D_{app}, to the direction of the diffusion due to its dependence from the DK tensor which is more complex than the DT. This sensibility can be clearly seen in the figure 2.9 in which three different acquisition directions (phase, read, slice) are showed for both D_{app} and K_{app}. In fact, the D_{app} intensity pattern is more or less stable among the three directions, while the one of K_{app} changes significantly depending on the direction considered [26].

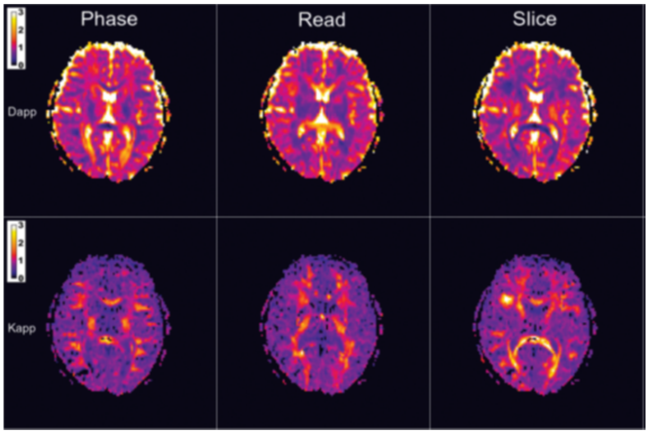

Figure 1.11: Phase, Read, Slice direction of D_{app} and K_{app} maps [26].

Given that the DKI model formulation includes both the estimation of the Diffusion and Diffusional Kurtosis tensors, the number of parameters to be computed is equal to 21, resulting from the 6 belonging to the DT to be added to the 15 just mentioned of the DK tensor. Therefore, with a suitable acquisition protocol that includes a multi-shell configuration with b-values ranging from below 1000 up to $3000 \frac{mm}{s^2}$, it is possible to provide a simultaneous assessment of both the diffusion metrics, already described in the previous paragraph, and the kurtosis metrics that are next to be discussed. As in DTI the indices of interest principally refer to the values associated to the three eigenvalues orientations and their mathematical combination, also in DKI the metric extraction approach is associated to the principal eigenvalues directions, except for the Mean Kurtosis (MK). In fact, the latter consists in an average measure of the different kurtosis values estimated for each sampling direction of the diffusion sensitizing gradients, resulting in:

$$MK = \frac{1}{n}\sum_{i=1}^{n}(K_{app})_i$$

where i is equal to the number of acquisition directions [25]. MK is believed to be generally proportional to the heterogeneity and complexity of the microstructure of the brain, where increased MK may indicate more densely packed cells or higher cellular complexity, and decreased MK may indicate loss of cellular structure. In addition to MK, it is possible to assess the magnitude of the kurtosis along the axial and radial direction of the major diffusion eigenvalue [27].

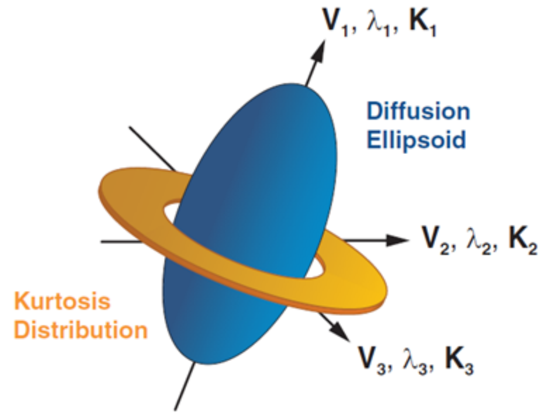

Figure 1.12: Kurtosis and Diffusion ellipsoids [27].

More specifically, assuming that K_1, K_2, K_3, are the kurtosis vectors along the corresponding DT eigenvector λ_i, the main kurtosis metrics that can be extracted correspond to the Axial Kurtosis (AK), defined as the kurtosis estimation along the principal eigenvalue, resulting in $AK = K_1$, and the Radial Kurtosis (RK) which is computed by averaging the two kurtosis contributions orthogonal to the principal diffusion direction, mathematically:

$$RK = \frac{K_2+K_3}{2}$$

RK is to be considered the main index of the DKI model useful to assess white matter structural coherence along with integrity of the cell membrane and surrounding myelin sheaths. The last kurtosis measure is the so-called Anisotropy Kurtosis (FA_K) that shares the same computation idea of the FA obtained from the DTI model, as it can be clearly noticed by its mathematical formulation given by:

$$FA_K = \sqrt{\frac{3}{2}\frac{\left(K_1-\bar{K}\right)^2+\left(K_2-\bar{K}\right)^2+\left(K_3-\bar{K}\right)^2}{K_1+K_2+K_3}}$$

in which $\bar{K}$ is the Mean Kurtosis. In this computation FA_K is determined only from three directional kurtosis estimates (K_1, K_2, K_3). To conclude, DKI offers a more comprehensive approach than DTI in describing the complex water diffusion process in vivo. By quantifying both mean and directional kurtoses and diffusivities, DKI may provide improved sensitivity and specificity in MR diffusion characterization of neural tissues [25].

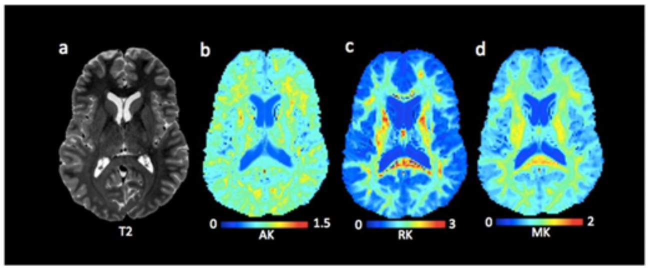

Figure 1.13: DKI parametrics maps [27].

1.2.3 DKI for glioma applications

Diffusion Kurtosis Imaging has been recently exploited to investigate the glioma behaviour in the brain microstructural environment and has proved to be a valid and efficient inspection tool. In fact, Jiang et al. demonstrated how DKI is able to assess the glioma grade and its proliferative activity. In 2015, they carried out DKI analysis and metrics extraction in a cohort of 74 patients with histopathological confirmed glioma. In this study, the relationships of these measures with the glioma grade and Ki-67 expression, which is a nuclear antigen expressed in proliferating cells that indicates cellular proliferation, were evaluated. Moreover, the diagnostic efficiency of DKI metrics in grading was further compared. It was demonstrated that compared with the conventional diffusion metrics, the kurtosis metrics were more promising imaging markers in distinguishing high-grade from low-grade gliomas and distinguishing among grade II, III and IV gliomas; the kurtosis metrics also showed great potential in the prediction of Ki-67 expression [28].

Soon after, Tonoyan et al. conducted a similar work, aiming to to assess the capabilities of diffusion kurtosis imaging in diagnosis of the glioma proliferative activity and to evaluate a relationship between the glioma proliferative activity index and diffusion parameters of the contralateral normal appearing white matter (CNAWM). In order to do so, the study included 47 patients with newly diagnosed brain gliomas, distributed in 23 low-grade, 13 grade III, and 11 grade IV gliomas. Then, they determined a relationship between absolute and normalized parameters of both diffusion tensor and diffusion kurtosis models, and the proliferative activity index in the most malignant part of the lesion. Their results showed that the correlation between all the absolute and normalized diffusion parameters and the glioma proliferative activity index was found to be statistically significant. These outcomes led to the conclusions that DKI has good capabilities to detect immunohistochemical changes in gliomas and demonstrated a high sensitivity in detection of microstructural changes in the CNAWM in patients with brain gliomas [29].

The following year, Li et al. provided a quantitative evaluation of histopathological changes in the microstructure at the center and periphery of glioma tumors using diffusional kurtosis imaging in a selection of 37 patients with diagnosticated cerebral gliomas. Correlations between normalized FA, MD, and MK and histopathological findings (tumor cell density, total vascular area [TVA], and Ki-67 labeling index [LI]) were assessed using Pearson correlation analyses. The results revealed that normalized MK exhibited the highest sensitivity (80%) and specificity (100%) in distinguishing HGGs from LGGs. Relative to the tumor center, normalized MK was significantly increased in the tumor periphery in LGGs and significantly decreased in HGGs, inferring that DKI, especially concerning the MK parameter, demonstrated high sensitivity in the detection of microstructural changes in patients with brain gliomas [30].

In another study, conducted by Hempel et al., the diagnostic performance of DKI for in vivo molecular profiling of human glioma was tested. The results of normalized MK and MD in 50 glioma patients were compared in regard to the WHO-based histological findings and molecular characteristics leading to integrated diagnosis. The main result of this work is that the diagnostic performance of MK seems to fit more with the integrated molecular approach than the conventional histological findings [31].

Lately, DKI has been extensively used to evaluate different glioma diffusion activity. Wu et al. focused on differentiating high-grade glioma recurrence from pseudo progression, comparing diffusion kurtosis imaging and diffusion tensor imaging. To do this, they recruited 40 patients with new enhancing lesions, specifically 24 high-grade glioma recurrence and 16 pseudo progression, and extracted both DTI and DKI parameters in the enhancing lesions and in the perilesional edema. This kind of analysis resulted to be very informative about DKI performances, showing how this imaging technique had superior performance in differentiating high-grade glioma recurrence from pseudo progression and relative MK appeared to be the best independent predictor [32].

Furthermore, Li et al. carried out a survival prediction analysis in glioblastoma (GBM) with Diffusion Kurtosis Imaging, aiming in particular to investigate whether any of the diffusion kurtosis parameters derived from is a significant predictor of overall survival. In this work, 33 GMB patients were included and both univariate and multivariate Cox models were used to evaluate the DKI parameters and clinical factors for prediction of overall survival (OS) and progression free survival (PFS). The DKI model demonstrated the potential to predict OS and PFS in the patients with GBM, inferring that further development and histopathological validation of the DKI model will warrant its role in clinical management of GBM [33].

Finally, Qiu et al. applied diffusion kurtosis imaging to the study of edema in solid and peritumoral areas of glioma. When gliomas grow in an infiltrative form, high-grade malignant glioma tissue extends beyond the contrast-enhancing tumor boundary, and this diffuse non-enhancing tumor infiltration is not visible on conventional MRI. In fact, the purpose of this study was to evaluate DKI-derived parameters in a group of 51 patients with pre-operative gliomas, assess changes in the solid tumor and peritumoral edema area and investigate the use of these measures for recurrence and prognosis estimation. In their work, DKI showed potential utility for studying solid tumor and peritumoral edema of high-grade gliomas, reporting significant differences between groups with grade III and IV gliomas in the peritumoral edema area, and correlation with clinical Ki-67 scores within the solid tumor area [34].

1.3 Graph Theory and Brain Network Analysis

1.3.1 Graph theory basic principles

Nowadays networks occur in very different scientific disciplines: economics, organizational studies, social sciences, biology, logistics, internet, and many others. Fortunately, the terminology that is used to describe the different networks in each discipline is largely the same, which makes it relatively easy for members of different communities to cooperate in understanding the foundations of complex networks. In addition, networks from very different fields often look so much alike. This common terminology and the strong resemblance of networks across scientific applications has been influential in boosting network science [35].

Network	**Vertices**	**Edges**
Airline Transportation	Airports	Flights
Train Transportation	Train Stations	Railways
World Wide Web (WWW)	Web pages	Hyperlinks
Internet	Routers	Cable connections
Citation	Authors	Citations
Genetic	Genes	Transcription factors
Brain	Neurons	Synapses

Table 1.1: Examples of networks [35].

The popular idea of network comes from the mathematical definition of graph. In fact, network science can be referred as graph theory equivalently. In order to introduce the basic concepts of networks, the fundamental formalities and notations from graph theory, together with a few fundamental properties that characterize networks, need to be explained. In its simplest form, a graph is a collection of vertices, also called nodes, that can be connected to each other by means of edges, or links. In particular, each edge of graph joins exactly two vertices. As mentioned before, the nodes and connections may represent people and their social relations, molecules and their interactions, or web pages and hyperlinks. Undirected graphs have edges that do not have a direction. The edges indicate a two-way relationship, in that each edge can be traversed in both directions. Contrarily, in a directed graph, also called digraph, all the edges are directed from one vertex, allowing connection only in the directions represented by the edges. If not specifically made explicit, usually the graph configuration considered is the one of undirected edges. V(G) and E(G) denote the set of vertices and edges associated with graph G, respectively. It is important to notice that an edge can be represented as an unordered tuple of two vertices, that is, its end points. For instance, $< u, v >$ defines an edge connecting vertices u and v, which is the equivalent formulation of $< v, u >$, since they both mean that the vertices taken into consideration are adjacent. In terms of links, loops and multiple edges connection, that is a set of edges each having u and v as their end points, are allowed. A graph without loops or multiple edges is called simple. As in so many practical situations, it is often convenient to talk about neighbors. In graph-theoretical terms, the neighbors of a vertex u are formed by the vertices that are adjacent to u [35].

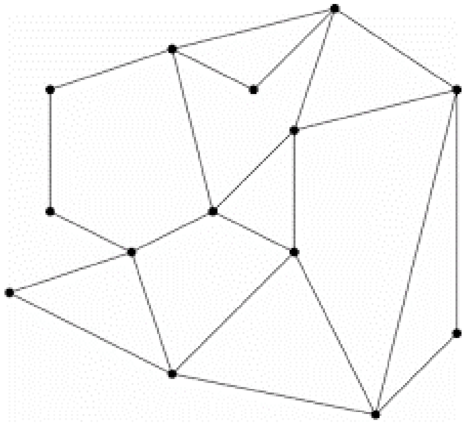

Figure 1.14: Graph topology [35].

An important property of a vertex is the number of edges that are incident with it. This number is called the degree of a vertex. In particular, a fundamental theorem of graph theory states that for all graphs G, the sum of the vertex degrees is twice the number of edges. The vertex degree is a simple, yet powerful concept and is used in many different ways, along with the degree distribution. For example, when considering social networks, we can use vertex degrees to express the importance of a person within a social group. Another important concept of graphs is that of a subgraph. A graph H is a subgraph of G if H consists of a subset of the edges and vertices of G, such that the end points of edges in H are also contained in H. There are different ways to represent graphs, especially when the representation must be suitable for automated processing. The most common one is to use an adjacency matrix. Consider a graph G with n vertices and m edges. Its adjacency matrix is nothing else but a table A with n rows and m columns with entry $A[i, j]$ denoting the number of edges joining vertex v_i and v_j [35].

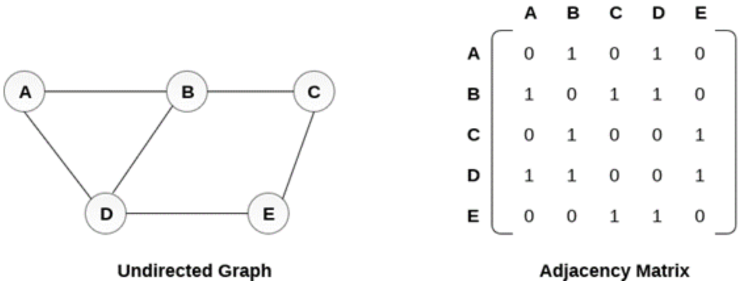

$$\begin{array}{c|ccccc} & A & B & C & D & E \\ \hline A & 0 & 1 & 0 & 1 & 0 \\ B & 1 & 0 & 1 & 1 & 0 \\ C & 0 & 1 & 0 & 0 & 1 \\ D & 1 & 1 & 0 & 0 & 1 \\ E & 0 & 0 & 1 & 1 & 0 \end{array}$$

Figure 1.15: Undirected graph and its corresponding adjacency matrix [36].

In a network, a path is defined as the set of edges and vertices through which a pair of nodes in linked. Using the notion of a path, a graph in considered to be connected when there is a path between each pair of distinct vertices. It is important to underline that, even if the vast majority of networks configuration is connected, there are some special cases in which there could be disconnected components of a graph. This means that a graph could also consist as a collection of components, where each component is a connected subgraph. The notion of connectivity is important, especially when considering the robustness of networks. Robustness in this context means how well the network stays connected when vertices or edges are removed. For instance, in the internet networks, it is a crucial ability to sustain serious attacks and failures such that connectivity is still guaranteed. Finding shortest paths, that is the shortest number of steps needed to link a pair of vertices, is a central problem in all networks. Fortunately, there exists an efficient algorithm (Dijkstra's algorithm) for computing the shortest paths from a given vertex u to all other vertices in a given undirected graph. It is important to highlight that there could be several shortest paths all having the same minimal length. In addition, another peculiarity of networks is to assign a weight to each edge, indicating some cost or strength in connections [35]. In order to extract meaningful information from networks' configurations, network analysis is exploited to compute specific connectivity metrics. Besides the already mentioned vertex degree and degree distribution, one of the most common estimates is the characteristic path length, also called average path length, defined as the average number of steps along the shortest paths for all possible pairs of network nodes. It is a measure of the efficiency of information or mass transport on a network. The clustering coefficient, which is a measure of the degree to which nodes in a graph tend to cluster together, is another principal measure that can be extracted from a graph. This concept is particularly important in scenarios of information spreading or epidemic dissemination and it is used also to classify networks. If weights represent the intensity by which, for example, interactions take place, then weights are also indicative for the strength, or looseness of a group. Another key metric for network analysis is deciding on whether there are any vertices "more important" than others. This concept of importance can be assessed by introducing the centrality measure. In a network, centrality can be computed by taking into consideration different aspects, which of course carry diverse information. The simplest centrality measure is the degree centrality (DC), which is defined by the number of connections attached to each node, calculated as:

$$k_i = \sum_{j=1}^{N} A_{ij}$$

in which A_{ij} are the adjacency matrix entries, equal to 1 if vertices i and j are linked, and N is the number of nodes in the network. Node centrality can also be defined in terms of the shortest paths. The distance between nodes i and j is given by the number of edges in the shortest path connecting them. A central node is close to all other nodes in the network in terms of this distance. This idea is enclosed in the closeness centrality measure, which is defined in terms of the average distance of each node to all others. Mathematically, the closeness centrality (CC) of node i is defined as:

$$C_i = \frac{N}{\sum_{j=1, j\neq i}^{N} d_{ij}}$$

where $d_{ij}$is the length of the shortest path between i and j. Closeness centrality has the advantage to be very intuitive and suitable to characterize a process in which the information travel through the shortest distances and it is more suitable when dealing with spatial networks. Another important centrality measure is the so-called betweenness centrality (BC), defined as the fraction of shortest paths, passing through a vertex i, connecting each pair of nodes. Analytically,

$$B_i = \sum_{a,b} \frac{\eta(a,i,b)}{\eta(a,b)}$$

in which $\eta(a,i,b)$ is the number of shortest paths connecting vertices a and b that pass transit over vertex i and $\eta(a,b)$ is the total number of shortest paths between a and b [36].

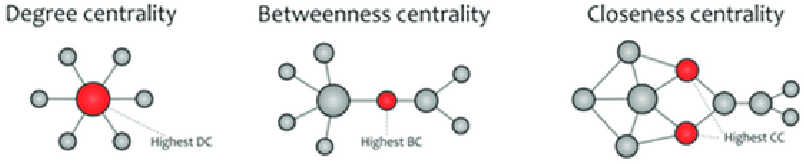

Figure 1.16: Graphical representation of centrality measures [37].

1.3.2 Brain complex networks

Nervous systems are the most complex networks known to man, capable of generating and integrating information from multiple external and internal sources in real time. Within the neuroanatomical substrate, the dynamics of neurons and neuronal activations result in patterns of statistical dependencies and causal interactions, defining three major modalities of complex brain networks: structural connectivity, functional connectivity, and effective connectivity. The first, also termed anatomical connectivity, is the set of physical or structural connections linking neuronal units at a given time. Anatomical connection patterns are relatively static at shorter time ratios but can be dynamic at longer time scales, for example during learning or development. Functional connectivity instead describes human cognition associated with rapidly changing and widely distributed neural activation patterns, which involve numerous cortical and subcortical regions activated in different combinations and contexts. Last, but not least, effective connectivity illustrates the set of causal effects of one neural system over another. Thus, unlike functional connectivity, requires the specification of a causal model including structural parameters. It is fundamental to underline the fact that structural, functional and effective connectivity are mutually interrelated. Clearly, structural connectivity is a major constraint on the kinds of patterns of functional or effective connectivity that can be generated in a network [38].

Most structural analyses of brain networks have been carried out to reveal several organizational principles. At the local level, simple statistical measures can be used to characterize inputs and outputs of individual areas. Such measures allow identification of highly connected nodes (hubs) and provide an initial functional characterization of areas as either ‘broadcasters’ or ‘integrators’ of signals. In addition, all large-scale cortical connection patterns exhibited small-world attributes with short path lengths and high clustering coefficients. The quantitative analysis of structural connection patterns using graph theory tools provides several insights into the functioning of neural architectures [38].

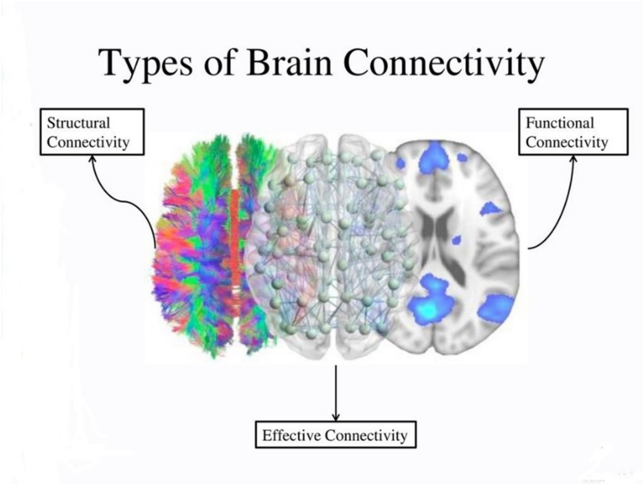

Figure 1.17: Types of brain connectivity [38].

The main aim of this kind of procedure is to build the so-called human connectome, which is mathematically defined as the connection matrix of brain. This allows not only for an inference from structural to functional connectivity, but also for a potential approach to capture the effects of developmental variations or abnormalities, traumatic brain injury, or neurodegenerative disease as specific structural variants of the human connectome [39].

Two major organizational principles of the cerebral cortex are functional segregation and functional integration, enabling the rapid extraction of information and the generation of brain states. Functional segregation in the brain is the ability for specialized processing to occur within densely interconnected groups of brain regions. Measures of segregation primarily quantify the presence of such groups, known as clusters or modules, within the network, having interpretations in anatomical and functional networks. The presence of clusters in anatomical networks suggests the potential for functional segregation in these networks, while the presence of clusters in functional networks suggests an organization of statistical dependencies indicative of segregated neural processing. The mean clustering coefficient for the network hence reflects, on average, the prevalence of clustered connectivity around individual nodes. More sophisticated measures of segregation not only describe the presence of densely interconnected groups of regions, but also find the exact size and composition of these individual groups. This composition is known as the network's modular structure, or community structure. On the other hand, functional integration in the brain is the ability to rapidly combine specialized information from distributed brain regions. Measures of integration characterize this concept by estimating the ease with which brain regions communicate and are commonly based on the concept of network path. The average shortest path length is the most commonly used measure of functional integration. The average inverse shortest path length is a related measure known as the global efficiency. More generally, the characteristic path length is primarily influenced by long paths, while the global efficiency is primarily influenced by short paths. Anatomical brain connectivity is thought to simultaneously reconcile the opposing demands of functional integration and segregation [39].

Furthermore, most studies examining functional brain networks also report various degrees of small-world organization. It is commonly thought that such an organization reflects an optimal balance of functional integration and segregation. Anatomical and effective networks are simultaneously highly segregated and integrated, and consequently have small-world topologies. In comparison, the functional network is also highly segregated but has a lower global efficiency, and therefore weaker small-world attributes. Concerning centrality, the degree centrality has a neurobiological interpretation: nodes with a high degree are interacting, structurally or functionally, with many other nodes in the network. The degree may be a sensitive measure of centrality in anatomical networks with nonhomogeneous degree distributions. Many measures of centrality are based on the idea that central nodes participate in many short paths within a network, and consequently act as important controls of information flow. In this context, the notion of betweenness centrality is naturally extended to links and could therefore also be used to detect important anatomical or functional connections [40].

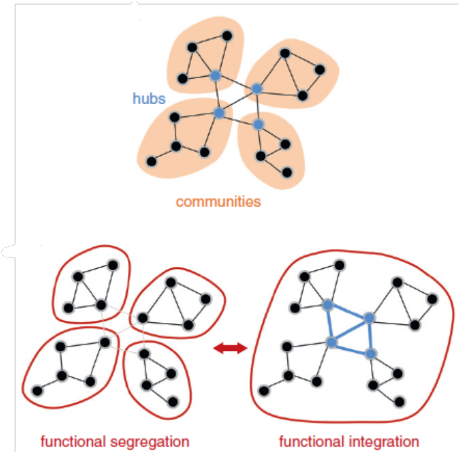

Figure 1.18: Brain network organizational principles [41].

Recent studies have demonstrated the existence of a number of highly connected and highly central neocortical hub regions, regions that play a key role in global information integration between different parts of the network, named 'brain hubs'. In particular, Sporns et al. conducted a study aiming to map out both the subcortical and neocortical hubs of the brain and examine their mutual relationship, particularly their structural linkages. Their results demonstrated that brain hubs form a so-called "rich club," characterized by a tendency for high-degree nodes to be more densely connected among themselves than nodes of a lower degree, providing important information on the higher-level topology of the brain network. These nodes are characterized by a high level of betweenness centrality and play a key role of functional hubs in optimizing global brain communication efficiency. These findings of a rich-club organization of the connectome provided new insight into how disorders affect brain topology and functioning, suggesting connectome alterations in a wide range of neurological and psychiatric brain disorders [42].

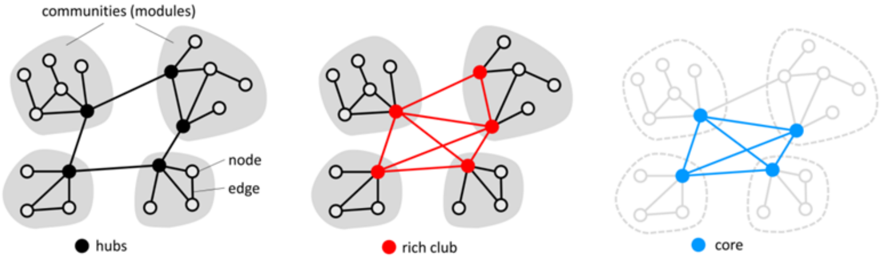

Figure 1.19: Rich club organization of the human connectome [42].

A number of emerging trends are the growing use of generative models, dynamic (time-varying) and multilayer networks. Starting from generative models, they are used for including statistical relevance and significance to the estimated measures of the network. In fact, null models that fix a number of different factors such as local node measures, spatial locations, and wiring cost effectively become generative models of the empirical data, able to account for topological features. Thus, generative models can provide important insights into the factors that have shaped the emergence of specific architectural or performance characteristics. Since brain networks are mutable model, it is important to consider time dependent factors, exploiting multilayer networks, that may influence the graph structure and metrics. Data on time varying brain graphs generally takes on the form of time series of graphs that form an ordered series of records, for example acquired while learning or across developmental stages. Changes in network topology can be tracked by computing graph measures on each time point, allowing the derivation of nodal measures of flexibility which can highlight parts of the network that are more variable across learning or development [43].

Finally, general developments in future will require conceptual efforts, particularly in the characterization of functional brain activity. One of the major challenges consists of better representing the functional space and improving the specificity of observed anatomical and dynamical networks associated with functional activity, and understanding which observed differences in network representations are neutral with respect to function. In addition, following complex network theory applications to neuroscience will demand that, instead of borrowing already available graph theoretical metrics designed to describe the brain connectome, neuroscientists should propose innovative network theory where the specific properties of the brain are taken into account. This means involving the brain's complex adaptive nature and redefining concepts in terms of not only distances but also community structures [44].

Chapter 2

Materials and Methods

2.1 MRI acquisition and pre-processing

Twenty patients suffering from de novo brain tumours have been recruited and acquired at the University Hospital of Padova from July 2017 to March 2021. All procedures were in accordance with the ethical standards of the institutional research committee and with the 1964 Helsinki declaration plus later amendments. All participants provided informed, written consent in accordance with the local University Hospital Institutional Review Board.

Data acquisition was performed with a 3T Siemens Biograph mMR-PET/MR scanner equipped with a 16-channels head-neck coil. The multi-shell dMRI protocol comprised a total of 100 diffusion weighted images (DWIs) (TR/TE 5355/104 ms; voxel size 2x2x2 mm3; FOV 220x220 mm2; 68 slices; multiband accelerator factor=2): 10 images at b=0 s/mm2, 30 DWIs at b-value=710 s/mm2 and 60 DWIs at b-value=2855 s/mm2. In addition, the acquisition protocol included anatomical imaging, which comprised a 3D T2-weighted (T2w) Fluid Attenuated Inversion Recovery (FLAIR) image (TR/TE 5000/395 ms; voxel size 1x1x1 mm3; FOV 250x250 mm2), two 3D T1-weighted (T1w) magnetization-prepared rapid acquisition gradient echo (MPRAGE, TR/TE 2400/3.2 ms; voxel size 1x1x1 mm3; FOV 256x256 mm2; 160 slices) acquired both before and after contrast agent injection and a T2w image (TR/TE 3200/536 ms; voxel size 1x1x1 mm3; FOV 256x256 mm2; 160 slices). The anatomical images of each patient were linearly registered to the patient naïve T1w image with the Advanced Normalization Tools (ANTs (Avants et al. 2011), v. 2.0.1). Employing these images, two masks were manually delineated through the ITK-SNAP software (http://www.itksnap.org/) by an expert neuroradiologist with more than five years of experience. The first mask, the T, included the tumour core (contrast agent enhancing and non-enhancing regions) and the necrosis, where present. The second mask, the T+O, was created by adding the oedema area to the T mask. In addition, each tumour was labelled by the same neuroradiologist as left, right or bilateral according to the location of its core and to the mainly involved hemisphere [45].

- *Diffusion MRI Pre-processing:* The acquired diffusion weighted volumes were visually inspected to identify and remove those images affected by interslice instabilities (J. D. Tournier, Mori, and Leemans 2011) which were deemed excessively corrupted for subsequent pre-processing techniques to correct. The rest of the preprocessing was executed in its entirety within the MRtrix3 Software (J.-D. Tournier et al. 2019) and was featured by an initial denoising step based on random matrix theory (Veraart, Fieremans, and Novikov 2016), and a subsequent call to the tools TOPUP (Andersson, Skare, and Ashburner 2003) and eddy (Andersson and Sotiropoulos 2016) from the FMRIB Software library (FSL) for B0 inhomogeneity, eddy current and motion joint correction. T1w segmentation results (including GM, subcortical parcellation, lesion and tumour masks) were registered to the naïve B0 volume using ANTs, by applying an affine transformation previously estimated on the patient's naïve T1w image.
- *Diffusion Tractography specifications:* The patient structural connectome reconstruction was performed in its entirety within the MRtrix3 software. We firstly performed multi-shell multi-tissue spherical deconvolution (Jeurissen et al. 2014) to recover the orientation distribution functions for each voxel. Subsequently, we computed the structural connectome by employing Anatomically Constrained Tractography (R. E. Smith et al. 2012), tracking individual fibres with a second-order Integration over Fiber Orientation Distributions algorithm (J.-D. Tournier, Calamante, and Connelly 2010). Standard streamline termination criteria values were used. The number of generated streamlines for each patient initially amounted to 100M, which were quantitatively reduced to 10M via the Spherical-deconvolution Informed Filtering of Tractograms framework (R. Smith et al. 2013) [45].

2.2 DKI estimation algorithms

In order to extract the Diffusion Kurtosis metrics, different estimation algorithms are used relying on both linear and non-linear methods. Specifically, the former refers to the Weighted Least Squares (WLS) implementation and the latter to the Non-linear Least Squares (NLS) computation. Usually, the non-linear approaches lead to a better fit of the model with the acquired data. The WLS used to be preferred for its simplicity and speed, but with the recent increase of computational power the NLS is more exploited than before. In fact, many variants of the WLS have been proposed in order to reduce the calculation burden and at the same time be competitive with the NLS method, which is known to be very slow but also robust against outliers. In this project, a standard WLS framework is compared to a regularized NLS algorithm. Analytically, the weighted linear estimator is defined as:

$$\beta = (X^T W X)^{-1} X^T W y$$

in which β represent the model parameters to be estimated, y refers to the acquired data, W is the weighting matrix, built as a diagonal matrix with $diag(W) = y^2$, and finally X consists in the so-called design matrix, which contains all the acquisition information regarding the diffusion gradient strengths and directions. Focusing on the β term, it is important to specify that it includes 15 variables, which compose the diffusion kurtosis tensor, and the S(0) image that shows the signal approximation without the diffusion sensitizing gradients [46].

Moving forward to the non-linear approach, the regularized NLS, it is an innovative methodology to compute the DKI model parameters involving a scalar kurtosis index to regularize the fit. First of all, this kind of implementation extracts the powder average signal of the dMRI, which is computed as:

$$logS(b) = S_{b=0} - b\dot{D} + \frac{1}{6}b^2\dot{D}^2\dot{K}^2$$

where $\dot{D}$ and $\dot{K}$ are the contribution of the scalar diffusion and excess kurtosis of powder signals, respectively. It is meaningful to underline the fact that from these scalar measurements does not allow for the estimation of directional diffusion and kurtosis values. From this data manipulation, the following step regards a robust mean kurtosis estimation, without relying on the full diffusion kurtosis tensor. For finite b-values, a mean kurtosis prediction can be obtained from $\dot{K}$ and the diffusion tensor $\bar{D}$ using a polynomial regression model in which the thousands of non-problematic voxels, that is, positive apparent kurtosis in each direction, serve as training data. In this strategy, called Voxel Quality Transfer, the polynomial coefficients are estimated using a multivariate polynomial regression defined as:

$$\hat{K} = P_n(\dot{K}, \bar{D}, \delta | C_n)$$

in which $\dot{K}$ is the predicted mean kurtosis, $\bar{D}$ is the whole diffusion tensor, δ is a linear combination of the $\bar{D}$ matrix components and C_n are the polynomial coefficients [47].

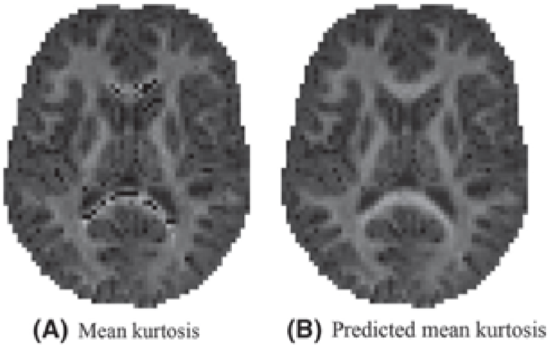

(A) Mean kurtosis **(B)** Predicted mean kurtosis

Figure 2.1: Mean Kurtosis VS Predicted Mean Kurtosis [47].

The next step is the definition of the non-linear fitting estimator, which analytically is designed as:

$$\hat{\theta} = argmin_{\theta}(||S - exp(B\theta)^2|| + \alpha||h(\theta) - \hat{K}||^2)$$

where α is the regularization weight and $h(\theta)$ the operator that computes the true mean kurtosis $\bar{K}$ from the tensor coefficients $\hat{\theta}$. For $\alpha = 0$, the estimator reduces to the ordinary NLS estimator, a widely adopted estimator for DTI and DKI. The nonlinear fitting is initiated by a starting point obtained by fitting the DKI model using the ordinary NLS estimator. It is important to underline that the L2 norm of the difference between K and K regularizes and stabilizes the DKI fit. By default,

$$\alpha = 0.1 \cdot \frac{MSE_{NLS}}{MSE_{MK}}$$

where the numerator is the median squared error of the standard NLS, and the denominator is the median squared error of the MK prediction carried out by the polynomial regression [47].

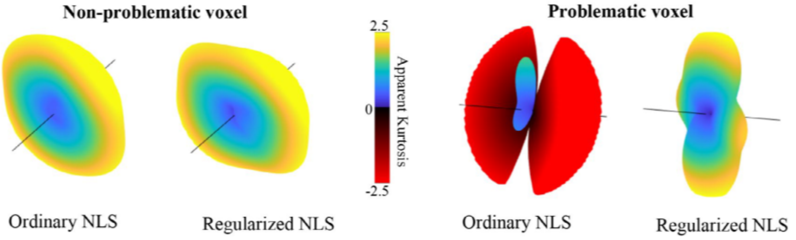

Figure 2.2: Kurtosis geometry: Non- Problematic VS Problematic voxel [47].

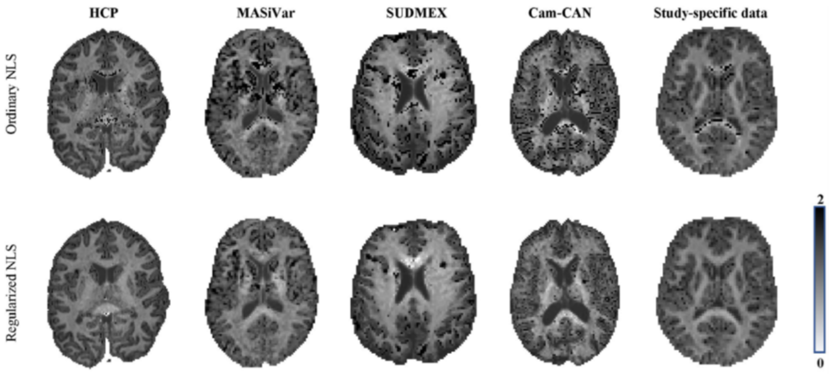

Figure 2.3: Ordinary VS Regularized MK estimation [47].

More recently, Kerkelä et al. provided an optimized version of this regularized NLS fit, exploiting the same strategy of the previously mentioned approach, but with a different Mean Kurtosis prediction method. In fact, in place of the polynomial regression estimation algorithm, they implemented a Multi-Layer Perceptron (MLP). The key role of this neural network is to learn MK, AK and RK predicted maps from data in voxels where the standard NLS was successful, and then use these estimates in the denominator of the formulation mentioned above. In such manner, the computation of the regularization weight of the following regularized NLS is informed by a more robust prediction algorithm, allowing for more reproducible results. The MLP architecture consists in a fully-connected feed-forward neural network with rectified linear units as activation functions. The network has an input layer size equal to the number of acquisitions, three hidden layers with 50 neurons each, and an output layer with size 3 (MK, AK and RK prediction). The initial weights are randomly generated with a hard-coded pseudorandom number generator seed. The loss function chosen is the mean squared error and Adam is used as the optimizer, with batch size equal to 200. The training is stopped when the loss does not improve by more than $10^{(}-4)$ for 10 consecutive epochs and this training procedure is repeated for each scan [48].

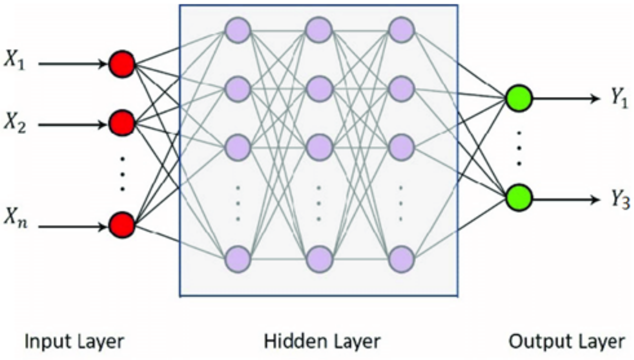

Figure 2.4: MLP architecture for MK, AK and RK maps prediction [48].

The final parameter estimates were obtained by solving the following optimization problem using Broyden-Fletcher-Goldfarb-Shanno (BFGS) algorithm:

$$\hat{\beta} = argmin_{\beta}\Bigg(\frac{1}{N}||S - exp(X\beta)||_2^2 + \alpha\Bigg((\hat{MK} - m(\beta))^2 + (\hat{AK} - a(\beta))^2 + (\hat{RK} - r(\beta))^2\Bigg)\Bigg)$$

in which $\hat{MK}$, $\hat{AK}$ and $\hat{RK}$ are the predicted kurtosis values, α is a constant controlling the magnitude of the regularization terms, and $m(\beta)$, $a(\beta)$, and

$r(\beta)$ are functions for numerically computing mean, axial, and radial kurtosis, respectively [48].

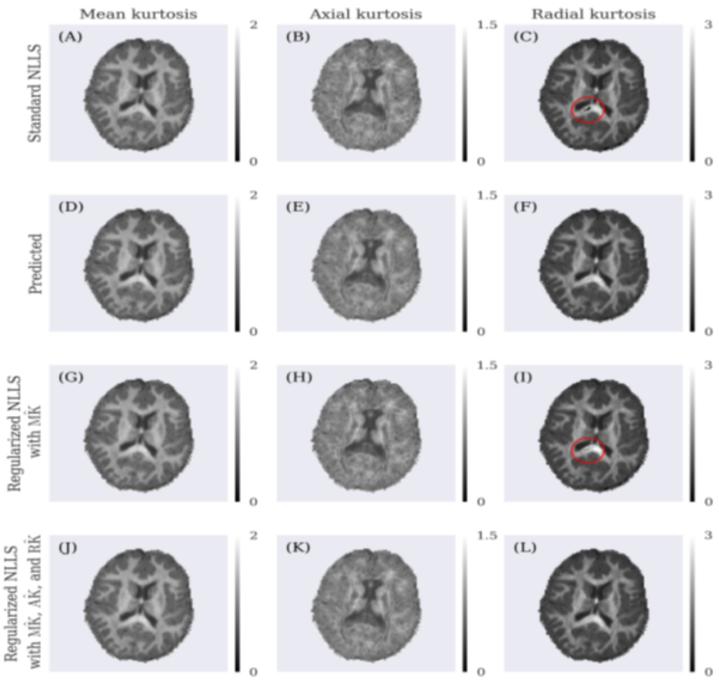

Figure 2.5: DKI parameter maps of different estimation algorithms [48].

2.3 DKI metrics sensibility analysis

From the literature it has been proved that some DTI metrics, such as the ADC or FA, are useful as biomarker for distinguishing not only different glioma grades, but also for separating the tumoral and periturmoral areas from the Normal Appearing White Matter (NAWM) tissue [28]. In this project, thanks to the innovative DKI model implementation, a tumor-specific sensibility analysis is carried out in order to verify whether both the principal diffusion and kurtosis indices are valuable informative measures to characterize different diseased tissues belonging to the tumoral area and to possibly identify a preferential spreading direction or pattern. In particular, the metrics of interest are the Fractional Anistropy and Mean Diffusivity as diffusion metrics, while Mean Kurtosis and Radial Kurtosis were considered as the diffusion kurtosis reference values.

Regarding the subdivision of the tumoral regions, the different tissues identified are labelled as:

- Necrosis region: is the death of brain tissue. It occurs when too little blood flows to the tissue and cannot be reversed.
- Tumor enhancing region: refers to the uptake of Gadolinium-based contrast agent in the lesion, meaning an increased vasculaziration or inflammation or angiogenesis [49].
- Tumor non-enhancing region: areas of increased T2 signal intensity associated with mass effect and architectural distortion such as blurring of the gray-white interface [50].
- Oedema region: concerns the swelling of the brain. Cerebral edema categorizes into either vasogenic, cellular, osmotic, and interstitial causes. It can arise from a variety of causes, including head trauma, vascular ischemia, intracranial lesions. The consequences of cerebral edema can be devastating, even fatal, if untreated [51].

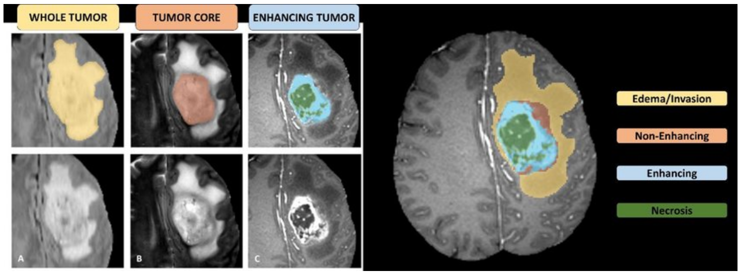

Figure 2.6: Glioma tumoral sub-regions. [52].

In order to carry out an accurate and effective analysis, only the subjects with 3 and 4 different tumor region masks were selected. For each of the considered areas, boxplots of FA, MD, MK and RK metrics were computed to evaluate not only the specific region values, but also the tumor region value distribution.

2.4 DKI metrics network analysis

Thanks to the creation of the diffusion and diffusion kurtosis maps for the selected subjects, it was possible to conduct a network analysis based on the DKI microparameters. The methodology to carry out this kind of investigation is described in this section. First of all, the brain cortical tissue has been divided according to the Schaefer atlas, which consist in a functional atlas. Specifically this operation is called brain parcellation and the atlas employed includes 7 functional networks that comprehend a 200 region parcellation of cortical brain regions, equally divided between the left and right hemispheres of the brain. The networks identified by resting-state functional MRI (rs-fMRI) investigation studies [53] are:

- Visual
- Default
- Control
- Somato-Motor
- Dorsal-Attention
- Ventral-Attention
- Limbic

For each subject and for each cortical region, the average value of diffusion and diffusion kurtosis metrics was extracted in order to build an association matrix of size 10 by 200, in which the rows represents the different subjects and the columns the mean value of the metric under investigation for each of the cortical regions considered. After that, the metrics connectivity matrices were computed by calculating the correlation index across the columns of the association matrix mentioned before. This operation returns a 200 by 200 connectivity matrix in which each entry correspond to the correlation index of a cortical region with another one, avoiding the self-correlation computation by setting the diagonal values equal to zero. The following procedure consisted in creating some sparsity in the microparameters correlation matrices built before, by applying a correction strategy that implies keeping only the correlation values that returned a p-value lower or equal to 0.05. These last sparse matrices were used as the adjacency matrices of the brain diffusion microparameters networks, for which the main centrality measures of degree, betweenness and eigenvector were determined in order to evaluate the connection behaviour of the networks considered, taking into consideration also the nodes' funtional network belonging.

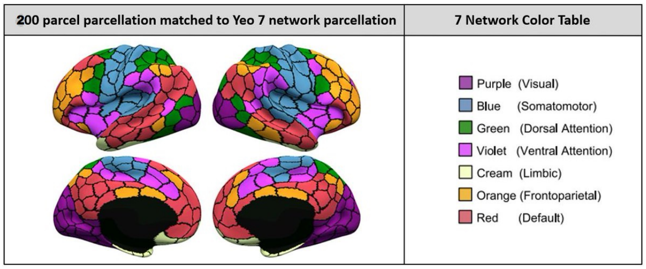

Figure 2.7: Brain Scheafer parcellation and functional networks.

Chapter 3

Results

3.1 Sensibility analysis

The total number of subjects for which the sensibility analysis was performed is equal to 10. In particular, the first four had 3 different tumoral tissue type masks, corresponding to Tumor Enhancing, Non-enhancing and Oedema, while the other six allowed to have a complete overview of the considered metrics over the 4 tumor tissue types, with the added Tumor Necrosis region. It has to be highlighted also the fact that the results are influenced also by the sizes of the masks of the different tumoral tissue type, which is different for every subject, given that the tumor behaviour is subject-dependent.

Starting from the first subject investigated, the boxplots of the diffusion metrics, both revealed a clear distinction of Tumor Non-enhancing region from the regions of Tumor Enhancing and Oedema areas. More specifically, FA and MD were not able to separate the Tumor Enhancing and Oedema regions, both in terms of difference in values and distribution. Taking into consideration the kurtosis indices instead, there is a slight differentiating capability for the Tumor Enhancing region from the other Non-enhancing and Oedema zones. In this case, MK and RK boxplots are very similar to each other, showing how the value distribution of the Tumor Oedema area is much different compared to the Enhancing and Non-enhancing sections.

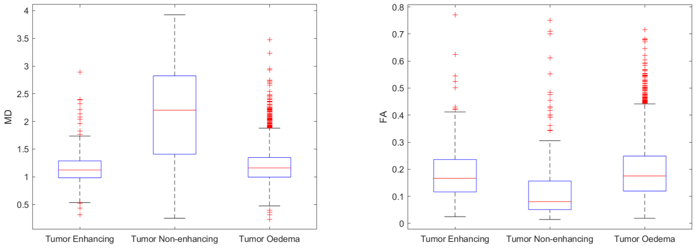

Figure 3.1: Subject 1 MD and FA region-specific tumor boxplots.

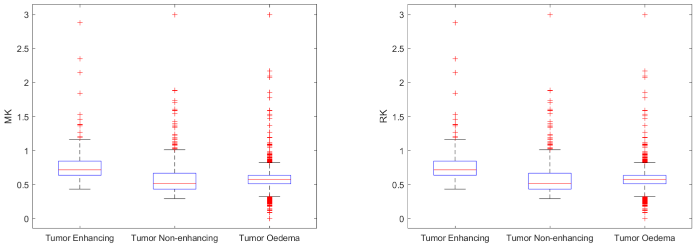

Figure 3.2: Subject 1 MK and RK region-specific tumor boxplots.

Metric	**Enhancing**	**Non-Enhancing**	**Oedema**
Subject 1	Median ± std	Median ± std	Median ± std
FA	0.166 ± 0.076	0.079 ± 0.077	0.175 ± 0.079
MD	1.122 ± 0.224	2.203 ± 0.727	1.160 ± 0.237
MK	0.717 ± 0.158	0.514 ± 0.217	0.575 ± 0.088
RK	0.719 ± 0.157	0.511 ± 0.205	0.572 ± 0.107

Table 3.1: Subject 1 sensibility table.

For the second individual considered, the trend of both diffusion and kurtosis metrics is very similar to the previous subject, with some marginal differences. In fact, MD and FA boxplots are more capable of distinguishing the three tumoral regions, even if with a marginal variation from the precedent case, giving also information about the value distribution variability among the diseased tissue types. The same happens when evaluating the kurtosis metrics, for which the boxplots highlight not only the similarity of classification of MK and RK, but also the high dissimilarity of the distribution of the values in the three tissue involved.

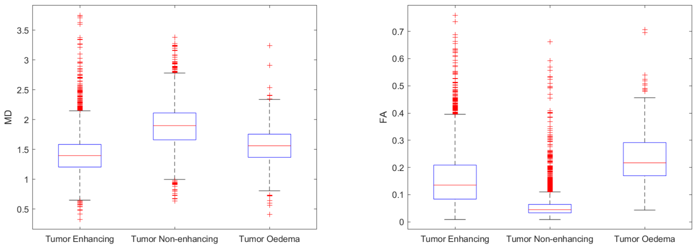

Figure 3.3: Subject 5 MD and FA region-specific tumor boxplots.

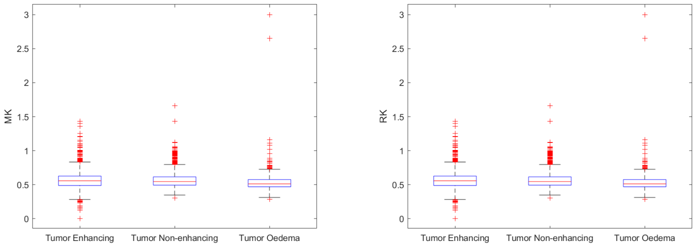

Figure 3.4: Subject 5 MK and RK region-specific tumor boxplots.

Metric	**Enhancing**	**Non-Enhancing**	**Oedema**
Subject 5	Median ± std	Median ± std	Median ± std
FA	0.135 ± 0.075	0.044 ± 0.031	0.216 ± 0.074
MD	1.397 ± 0.247	1.898 ± 0.274	1.562 ± 0.253
MK	0.555 ± 0.085	0.573 ± 0.079	0.511 ± 0.084
RK	0.560 ± 0.093	0.564 ± 0.084	0.537 ± 0.107

Table 3.2: Subject 5 sensibility table.

The third subject exhibited a different trend from the previous cases. In fact, regarding the diffusion metrics, it is evident that MD boxplots are not able to provide a significant separation among the different tissues and only carry information about the value distribution. Contrarily, FA seems to be a more valuable measure to distinguish the diverse tumoral tissue areas, but it is lacking in terms of distribution characterization. Concerning the kurtosis indices, they both produce a valuable division of the tumor region-specific tissue, even if some differences need to be underlined. In fact, MK furnish an acceptable differentiation of Tumor Non-enhancing region compared to Enhancing and Oedema areas, whose boxplots are very similar. RK instead allows for a complete distinction of all diseased tissue taken into consideration, resulting the most reliable sensibility index.

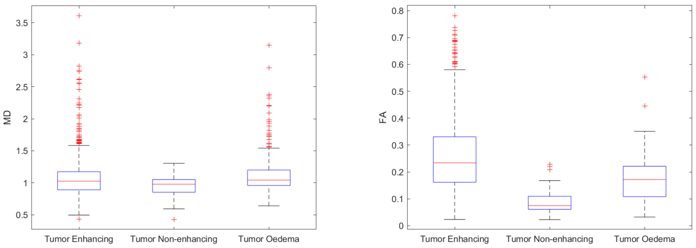

Figure 3.5: Subject 6 MD and FA region-specific tumor boxplots.

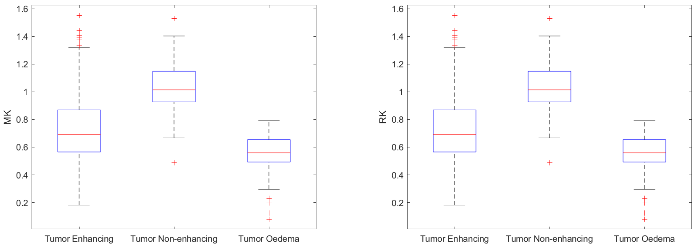

Figure 3.6: Subject 6 MK and RK region-specific tumor boxplots.

Metric	**Enhancing**	**Non-Enhancing**	**Oedema**
Subject 6	Median ± std	Median ± std	Median ± std
FA	0.233 ± 0.102	0.074 ± 0.032	0.172 ± 0.064
MD	1.025 ± 0.190	0.978 ± 0.130	1.042 ± 0.239
MK	0.690 ± 0.173	1.014 ± 0.135	0.559 ± 0.096
RK	0.740 ± 0.218	0.991 ± 0.125	0.556 ± 0.126

Table 3.3: Subject 6 sensibility table.

For the last subject with 3 different tumoral tissue types, diffusion metrics produce an effective diversification. In particular, MD is effectively distinguishing the Tumor Enhacing and Oedema regions and reveals a slight change between Tumor Non-Enhancing and Enhancing or Oedema zones. On the other hand, FA is even more sensible to provide an efficient distinction among all the tumor affected tissues. Regarding the kurtosis indices, it is evident that they provide the same differentiation performance. In fact, both MK and RK, cannot separate the tissue types in an acceptable manner, but they give important information about the value distribution in the diseased regions, highlighting a smaller variation range in the Tumor Oedema, accompanied by a higher number of outliers, compared to the Enhancing and Non-enhancing areas.

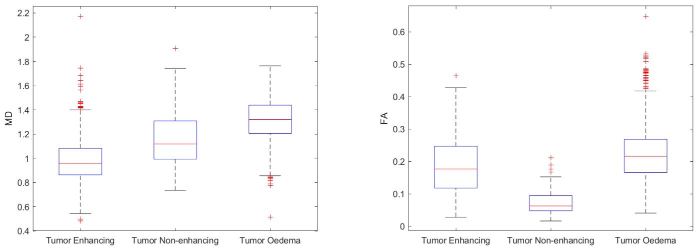

Figure 3.7: Subject 7 MD and FA region-specific tumor boxplots.

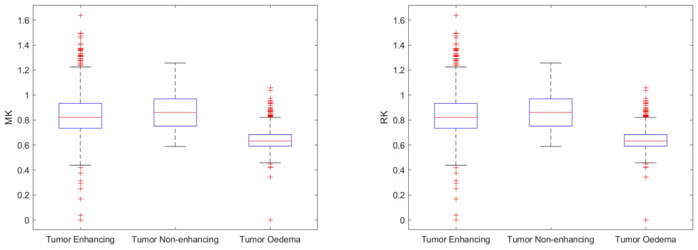

Figure 3.8: Subject 7 MK and RK region-specific tumor boxplots.

Metric	**Enhancing**	**Non-Enhancing**	**Oedema**
Subject 7	Median ± std	Median ± std	Median ± std
FA	0.176 ± 0.069	0.062 ± 0.031	0.216 ± 0.061
MD	0.958 ± 0.146	1.118 ± 0.194	1.320 ± 0.136
MK	0.821 ± 0.141	0.860 ± 0.124	0.632 ± 0.060
RK	0.905 ± 0.152	0.871 ± 0.139	0.736 ± 0.096

Table 3.4: Subject 7 sensibility table.

From now on, all the remaining included subjects show also the presence of the Tumor Necrosis. Starting from the first complete individual, the sensibility analysis showed that diffusion metrics can provide a valuable diversification. In fact, MD boxplots distinguish Tumor Necrosis, Enhancing and Non-enhancing regions, while producing only a slight change between Non-enhancing and Oedema areas. In addition, FA boxplots produce an even more accurate tumoral tissue differentiation, resulting to be a reliable sensibility index, showing a slight change only between Tumor Necrosis and Oedema zones. On the other hand, the kurtosis metrics exhibit more or less the same trend. In particular, MK shows a good distinction property among Tumor Necrosis, Enhancing and Non-enhancing regions, while presenting only a subtle contrast between Tumor Necrosis and Oedema areas. The same trend is showed by the RK boxplots.

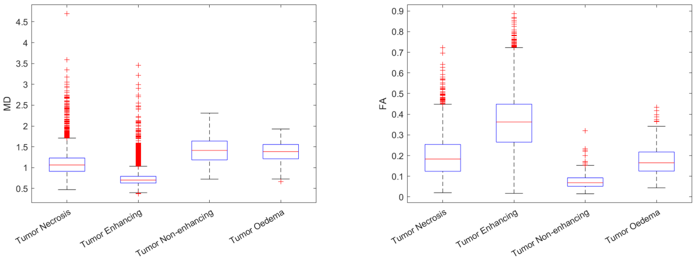

Figure 3.9: Subject 9 MD and FA region-specific tumor boxplots.

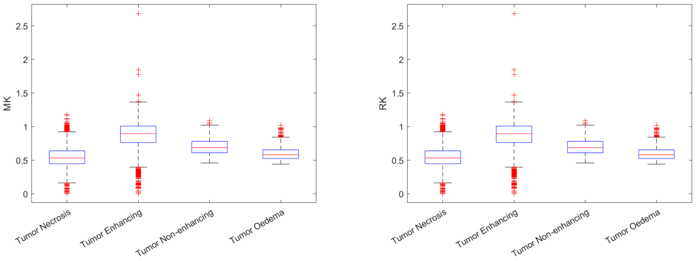

Figure 3.10: Subject 9 MK and RK region-specific tumor boxplots.

Metric	**Necrosis**	**Enhancing**	**Non-Enhancing**	**Oedema**
Subject 9	Median ± std	Median ± std	Median ± std	Median ± std
FA	0.183 ± 0.078	0.362 ± 0.108	0.068 ± 0.026	0.165 ± 0.056
MD	1.064 ± 0.236	0.702 ± 0.128	1.414 ± 0.255	1.384 ± 0.206
MK	0.534 ± 0.124	0.896 ± 0.152	0.688 ± 0.095	0.581 ± 0.090
RK	0.538 ± 0.163	1.012 ± 0.229	0.700 ± 0.104	0.604 ± 0.119

Table 3.5: Subject 9 sensibility table.

Moving to the next analysed subject, the kurtosis metrics showed a higher sensibility compared to the diffusion indices. In fact, MD is effective only for the diversification of the Tumor Non-enhancing region from the the other three tumoral tissues, and the same is happening for FA. Contrarily, MK and RK, which show more or less the same value and distribution of the different diseased tissues, are able to provide a reliable differentiation and may be used for the identification of the tumor region-specific tissue.

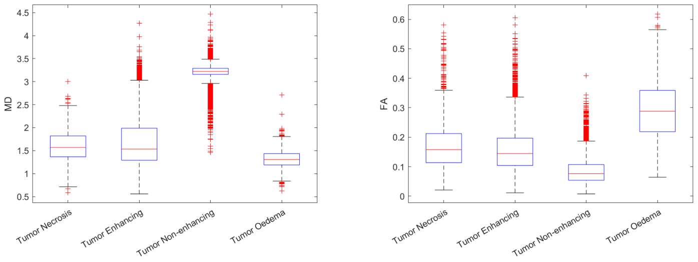

Figure 3.11: Subject 12 MD and FA region-specific tumor boxplots.

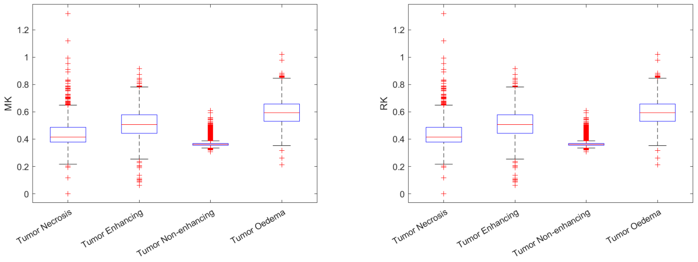

Figure 3.12: Subject 12 MK and RK region-specific tumor boxplots.

Metric	**Necrosis**	**Enhancing**	**Non-Enhancing**	**Oedema**
Subject 12	Median ± std	Median ± std	Median ± std	Median ± std
FA	0.157 ± 0.060	0.144 ± 0.060	0.076 ± 0.035	0.288 ± 0.078
MD	1.568 ± 0.253	1.534 ± 0.455	3.221 ± 0.120	1.306 ± 0.153
MK	0.415 ± 0.067	0.507 ± 0.074	0.361 ± 0.011	0.593 ± 0.075
RK	0.420 ± 0.081	0.521 ± 0.086	0.356 ± 0.014	0.652 ± 0.111

Table 3.6: Subject 12 sensibility table.

In the following subject, the metrics sensibility quite resembles the situation seen for the previous individual. In fact, the only valuable differentiation showed by MD boxplots is the one of the Tumor Non-enhancing region from the other three tumor areas. However it has to be highlighted the fact that the Tumor Oedema also can be considered distinct from the others in an acceptable way. For the FA index, the same considerations of MD can be draw, showing an even worse performance. On the other hand, kurtosis metrics exhibit a similar classification between each other. Precisely, both MK and RK boxplots reveal significant differences in the Tumor Non-enhancing area compared to the remaining three tissues, with a slight distinction of the Tumor Oedema zone. In this case, diffusion and kurtosis indices provide the same diversification interpretation.

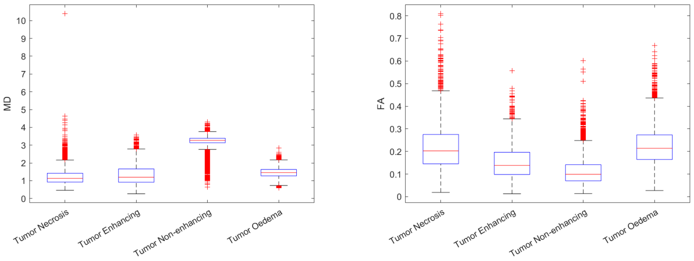

Figure 3.13: Subject 14 MD and FA region-specific tumor boxplots.

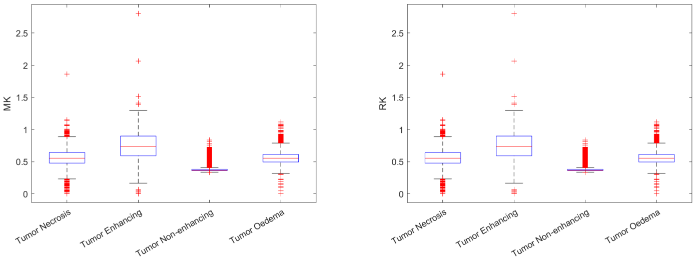

Figure 3.14: Subject 14 MK and RK region-specific tumor boxplots.

Metric	**Necrosis**	**Enhancing**	**Non-Enhancing**	**Oedema**
Subject 14	Median ± std	Median ± std	Median ± std	Median ± std
FA	0.202 ± 0.078	0.138 ± 0.059	0.098 ± 0.048	0.213 ± 0.065
MD	1.133 ± 0.339	1.194 ± 0.476	3.267 ± 0.307	1.454 ± 0.218
MK	0.552 ± 0.107	0.736 ± 0.168	0.366 ± 0.036	0.552 ± 0.074
RK	0.552 ± 0.137	0.732 ± 0.160	0.372 ± 0.042	0.577 ± 0.112

Table 3.7: Subject 14 sensibility table.

The trend of the diffusion metrics for the next subject is quite similar to the precedent case. In fact, MD and FA boxplots are able to show a significant distinction only for the Tumor Non-enhancing zone, while the Tumor Oedema exhibits only a different value distribution. Contrarily, kurtosis metrics can assess two different groups of tissues. Specifically, MK and RK boxplots identify a valuable separation between the two couples of tumoral tissue composed by Tumor Necrosis and Enhancing, and Tumor Non-enhancing and Oedema. In this case, RK results to be slightly more sensible compared to MK.

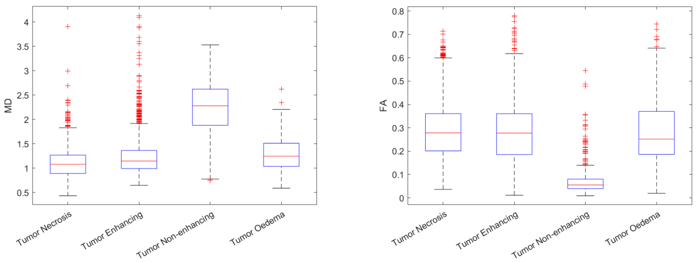

Figure 3.15: Subject 17 MD and FA region-specific tumor boxplots.

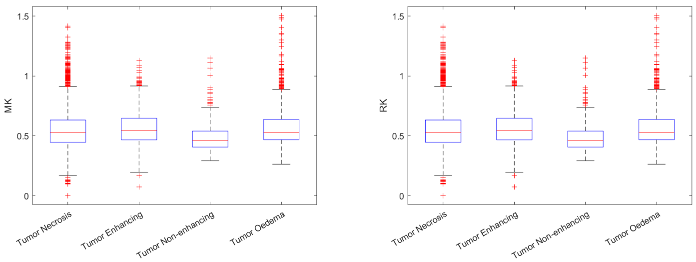

Figure 3.16: Subject 17 MK and RK region-specific tumor boxplots.

Metric	**Necrosis**	**Enhancing**	**Non-Enhancing**	**Oedema**
Subject 17	Median ± std	Median ± std	Median ± std	Median ± std
FA	0.278 ± 0.091	0.277 ± 0.101	0.055 ± 0.038	0.251 ± 0.104
MD	1.081 ± 0.211	1.146 ± 0.253	2.280 ± 0.449	1.246 ± 0.252
MK	0.528 ± 0.122	0.544 ± 0.108	0.460 ± 0.087	0.526 ± 0.107
RK	0.533 ± 0.158	0.588 ± 0.129	0.462 ± 0.097	0.543 ± 0.152

Table 3.8: Subject 17 sensibility table.

For the following individual, diffusion metrics are to be considered more reliable compared to the kurtosis ones. In fact, both MD and FA can distinguish the Tumor Enhancing and Non-enhancing regions from the rest of the tumoral tissue. A subtle change also can be noted between Tumor Necrosis and Oedema, but not significant. Concering the kurtosis metrics instead, MK and RK are both only able to separate the Tumor Non-enhancing area from the other ones, and only slight differences can be noted among the Tumor Necrosis, Enhancing and Oedema zones.

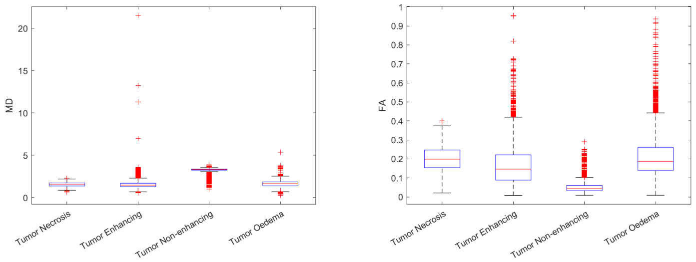

Figure 3.17: Subject 19 MD and FA region-specific tumor boxplots.

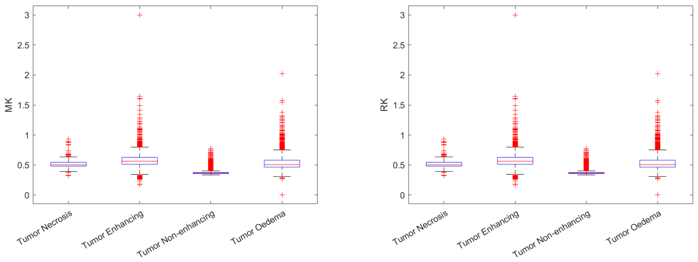

Figure 3.18: Subject 19 MK and RK region-specific tumor boxplots.

Metric	**Necrosis**	**Enhancing**	**Non-Enhancing**	**Oedema**
Subject 19	Median ± std	Median ± std	Median ± std	Median ± std
FA	0.198 ± 0.052	0.146 ± 0.077	0.043 ± 0.020	0.187 ± 0.083
MD	1.558 ± 0.221	1.459 ± 0.305	3.303 ± 0.223	1.648 ± 0.281
MK	0.504 ± 0.042	0.562 ± 0.071	0.363 ± 0.026	0.505 ± 0.083
RK	0.535 ± 0.041	0.562 ± 0.076	0.375 ± 0.027	0.562 ± 0.137

Table 3.9: Subject 19 sensibility table.

The last included subject shows a similar differentiation trend compared to the previous individual. In fact, MD only provides a significant distinction for the Tumor Non-enhancing region, while FA is effectively differentiating both Tumor Non-enhancing and Oedema areas. Regarding the kurtosis metrics, which show a similar value distribution trend, are able to separate the Tumor Necrosis and Enhancing tissues, while there is only a change between Tumor Non-enhancing and Oedema zones in terms of value distribution.

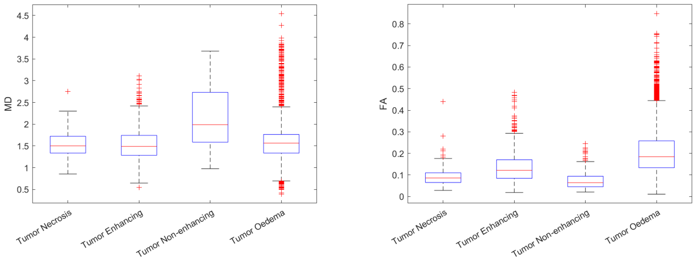

Figure 3.19: Subject 20 MD and FA region-specific tumor boxplots.

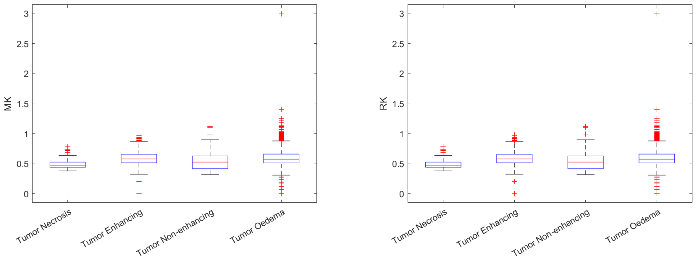

Figure 3.20: Subject 20 MK and RK region-specific tumor boxplots.

Metric	**Necrosis**	**Enhancing**	**Non-Enhancing**	**Oedema**
Subject 20	Median ± std	Median ± std	Median ± std	Median ± std
FA	0.085 ± 0.031	0.121 ± 0.055	0.064 ± 0.035	0.184 ± 0.076
MD	1.501 ± 0.243	1.487 ± 0.298	1.988 ± 0.581	1.564 ± 0.264
MK	0.473 ± 0.054	0.579 ± 0.088	0.525 ± 0.123	0.574 ± 0.090
RK	0.504 ± 0.056	0.607 ± 0.101	0.548 ± 0.127	0.654 ± 0.139

Table 3.10: Subject 20 sensibility table.

3.2 Network analysis

The results of the microparameters network analysis are showed in this section. First of all, the diffusion and diffusion kurtosis connectivity matrices display an evident clustered configuration that reveals the different brain functional networks. In particular, this kind of pattern is more observable for MD and MK matrices that can well capture the diffusion dynamics in the gray matter cortical regions. Contrarily, FA and RK, being metrics of white matter integrity estimation, are less able to identify the brain functional block structures. However, the network analysis was carried out for all the metrics computed in order to inspect all the different possible insights each measure can provide. For each metric, network degree, betweenness and eigenvector centrality measures were extracted to identify brain hubs, bridges and the nodes with high transitive influence on others, respectively. For each of these network metrics, the top 5 high-scoring nodes were reported in tables to have also a functional reference for the different network configurations considered.

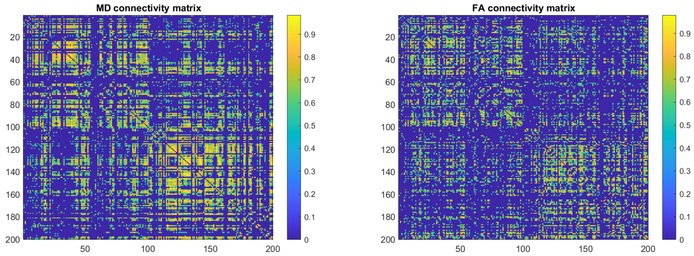
MD connectivity matrix

FA connectivity matrix

Figure 3.21: MD and FA region-specific connectivity matrices.

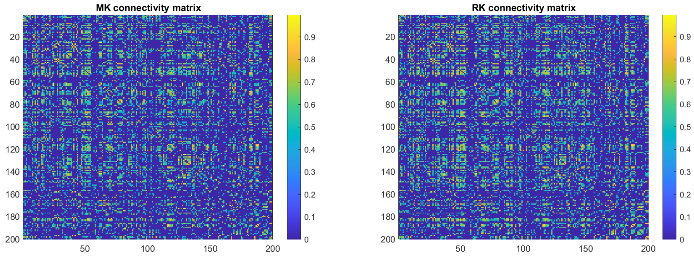
MK connectivity matrix

RK connectivity matrix

Figure 3.22: MK and RK region-specific connectivity matrices.

The first diffusion metric under investigation is FA. Starting from the measure of degree centrality, is clear that the main hub roles are played by the nodes belonging to the Dorsal and Ventral Attention networks. However, is important to include also regions of both Somato-Motor and Default networks. It is also worth to highlight the fact that four the top 5 scoring hubs are placed in the right hemisphere (RH) of the brain functional configuration.

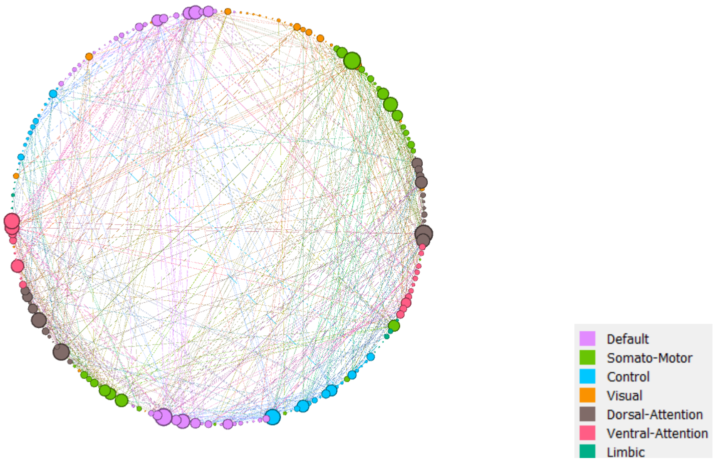

Figure 3.23: FA degree connectivity graph.

FA DEGREE CENTRALITY		
Top 5 Hubs	**Degree**	**Functional Network**
RH DorsAttn FEF 2	23	Dorsal-Attention
RH Default PFCdPFCm 7	22	Default
RH SomMot 4	22	Somato-Motor
LH DorsAttn Post 3	21	Dorsal-Attention
RH Cont PFCmp 2	20	Control

Table 3.11: FA connectivity degree centrality.

The situation for the betweenness centrality netowrk organization is similar to the one presented for the degree. In fact, the main functional bridges for FA connectivity are represented by regions belonging to the Dorsal-Attention networks. Certainly, it is meaningful to include also nodes of Default and Somato-Motor networks. As noted in the previous network configuration, also here four of the top 5 scoring nodes are associated to the RH area of the brain.

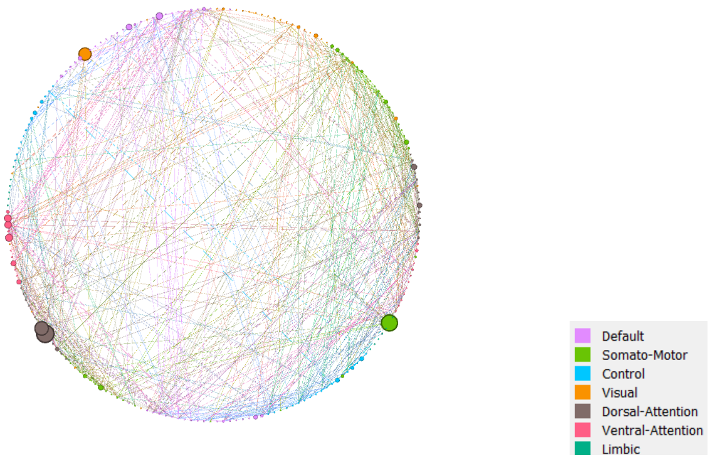

Figure 3.24: FA betweenness connectivity graph.

FA BETWEENNESS CENTRALITY		
Top 5	**Betweenness**	**Functional Network**
RH DorsAttn PrCv 1	1118	Dorsal-Attention
LH DorsAttn Post 3	1117	Dorsal-Attention
RH Default PFCdPFCm 7	1151	Default
RH SomMot 12	1128	Somato-Motor
RH DorsAttn FEF 2	992	Dorsal-Attention

Table 3.12: FA connectivity betweenness centrality.

Much different is the network configuration concerning the eigenvector centrality of the FA connectivity graph. In fact, here almost all functional networks are included in describing the influence of brain regions over others. Specifically, only the visual and limbic networks are excluded from contributing to delineate the eigenvector arrangement of the graph. As for the previous FA connectivity networks, the most involved nodes belong to the RH of the brain.

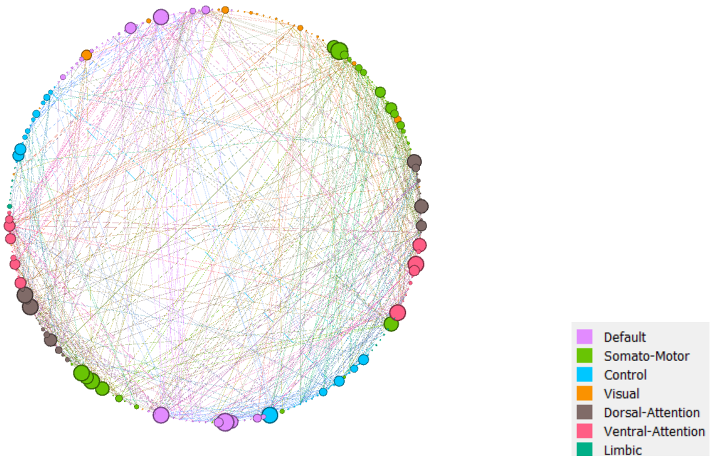

Figure 3.25: FA eigenvector connectivity graph.

FA EIGENVECTOR CENTRALITY		
Top 5	**Eigenvector**	**Functional Network**
RH DorsAttn FEF 2	1	Dorsal-Attention
RH Default PFCdPFCm 7	0.935	Default
RH SomMot 4	0.912	Somato-Motor
RH Cont PFCmp 2	0.905	Control
LH DorsAttn Post 3	0.851	Dorsal-Attention

Table 3.13: FA connectivity eigenvector centrality.

Considering the other diffusion metric under investigation, the MD connectivity network reveals different aspects compared to the FA results. In fact, by looking at the degree MD graph, it is evident that the major hub nodes belong to the Attention networks, both Dorsal and Ventral. In addition, it is remarkable to include also brain regions associated to the Somato-Motor and Default networks. In this case, it is possible to hypothesize that in glioma patients the Attention, Default and Somato-Motor functional networks activation could by synchronized, as for rs-fMRI data.

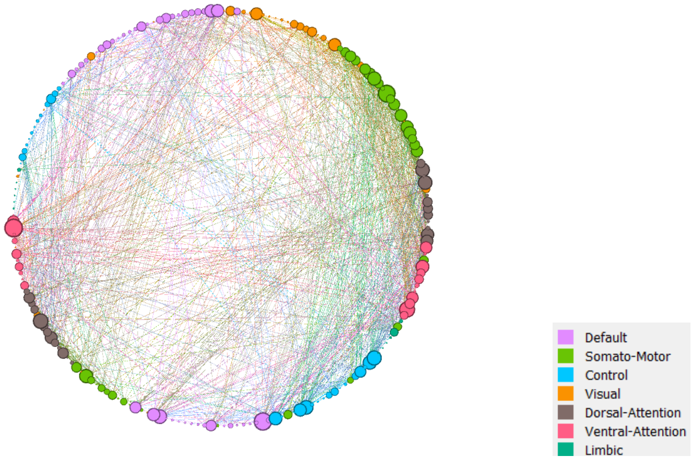

Figure 3.26: MD degree connectivity graph.

MD DEGREE CENTRALITY		
Top 5 Hubs	**Degree**	**Functional Network**
LH SalVentAttn Med 1	37	Dorsal-Attention
RH Default Par 2	36	Default
RH SomMot 10	35	Somato-Motor
RH SalVentAttn Med 2	31	Ventral-Attention
LH DorsAttn Post 9	30	Dorsal-Attention

Table 3.14: MD connectivity degree centrality.

Moving to the betwennees centrality measure extracted from the MD connectivity graph, it is clear from the graphical representation that the main bridge roles of the network are played by brain regions member of Ventral-Attention, Somato-Motor and Visual functional networks. In this case, it could be reasonable to infer that these areas are crucial for the exchange of information in the whole brain architecture. In addition, it is worth mentioning the importance of the Default and Dorsal-Attention nodes which are also relevant interchange vertices.

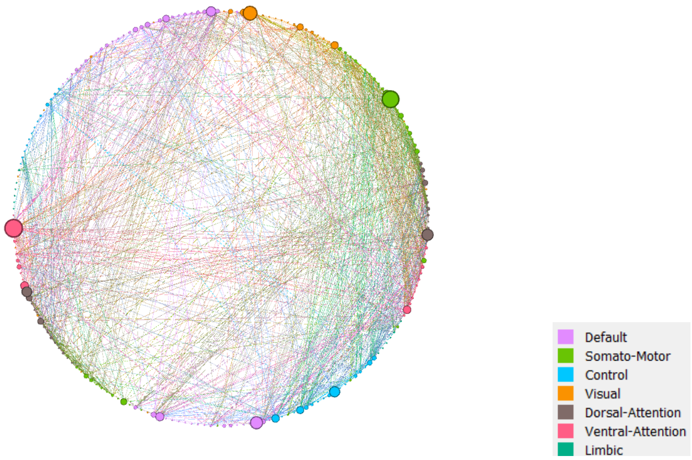

Figure 3.27: MD betweenness connectivity graph.

MD BETWEENNESS CENTRALITY		
Top 5	**Betweenness**	**Functional Network**
LH SalVentAttn Med 1	1340	Ventral-Attention
RH SomMot 11	1269	Somato-Motor
RH Vis 2	1029	Visual
RH Default Par 3	888	Default
RH DorsAttn FEF 2	805	Dorsal-Attention

Table 3.15: MD connectivity betweenness centrality.

Regarding the eigenvector centrality estimation extrapolated from the MD connectivity network, it has to be highlighted the fact that the most influent brain regions are mainly associated to Somato-Motor and Default functional networks. These results may suggest that these brain regions are to be considered the most important for the functional activation influence, originating a ripple stimulating effect also on the other functional connected networks and causing their partial activation. Along with the above mentioned networks, the Ventral-Attention and Control areas are to be included in the noteworthy findings, even if they have a minor contribution to the chain activation effects.

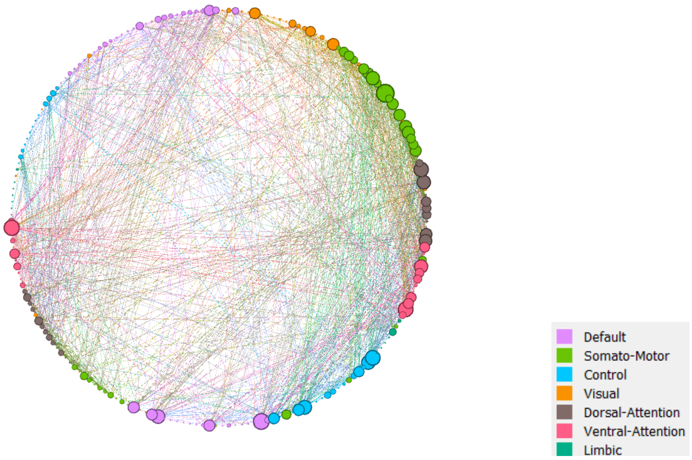

Figure 3.28: MD eigenvector connectivity graph.

MD EIGENVECTOR CENTRALITY		
Top 5	**Eigenvector**	**Functional Network**
RH SomMot 10	1	Somato-Motor
RH Default Par 2	0.884	Default
LH SalVentAttn Med 1	0.850	Ventral-Attention
RH SalVentAttn Med 2	0.825	Ventral-Attention
RH Cont Par 1	0.819	Control

Table 3.16: MD connectivity eigenvector centrality.

Moving to the kurtosis metrics, the MK connectivity graph reveals a similar hubs identification compared to the MD estimation. In fact, a part from the peculiar degree score, the most important nodes correspond with the same functional networks found in the MD graph, specifically the Dorsal and Ventral-Attention networks, along with Default and Somato-Motor functional areas. Contrarily to MD degree graph, for MK the top 5 scoring hubs principally belong to the brain left hemispher (LH), showing how the MK metric provides an integration of information concerning the brain network functional configuration. Also in this context it is possible to deduce that these regions could have synchronized activation similar to the one investigated in fMRI investigations.

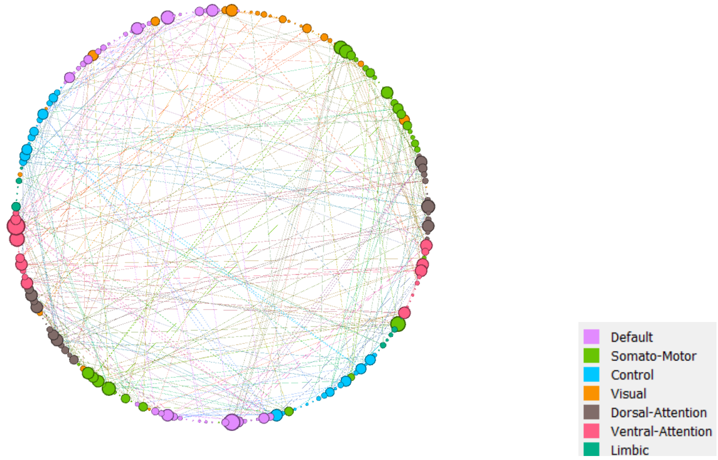

Figure 3.29: MK degree connectivity graph.

MK DEGREE CENTRALITY		
Top 5 Hubs	**Degree**	**Functional Network**
LH SalVentAttn Med 1	11	Dorsal-Attention
RH Default Temp 4	10	Default
LH SomMot 2	9	Somato-Motor
LH SalVentAttn FrOperIns 4	9	Ventral-Attention
LH SomMot 11	8	Somato-Motor

Table 3.17: MK connectivity degree centrality.

Considering the betweenness centrality measure extracted from the MK connectivity graph, it is interesting to underline the fact that the key bridges nodes belong mainly to the Dorsal-Attention, Somato-Motor and Visual functional networks. As hypothesised for MD, which shares a similar betweenness top 5 scoring regions, these areas may be the most involved in the information signal transfer through the entire brain network configuration. Differently from MD betweenness connectivity, here the Default network nodes are not significantly contributing to cover bridge roles in this type of architecture.

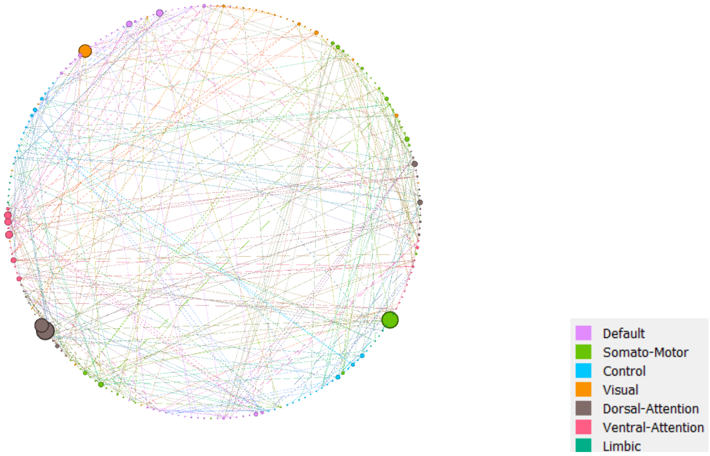

Figure 3.30: MK betweenness connectivity graph.

MK BETWEENNESS CENTRALITY		
Top 5	**Betweenness**	**Functional Network**
LH DorsAttn Post 6	1707	Dorsal-Attention
LH SomMot 2	1560	Somato-Motor
RH DorsAttn Post 7	1295	Dorsal-Attention
RH Vis 8	1170	Visual
LH SalVentAttn FrOperIns 4	614	Ventral-Attention

Table 3.18: MK connectivity betweenness centrality.

Contrarily to MD eigenvector results, in which the top 5 central nodes were distributed among four different functional networks, for MK there is an almost complete overtaking of the Somato-Motor functional network over the others. It is also clear from the graphical representation that the Limbic and Visual areas are not so influent in the activation pattern of the brain. On the other hand, the Default and Somato-Motor regions may be the mainly activation regulators of the brain functional activity, followed by the Attention networks, both Dorsal and Ventral, and the Control areas.

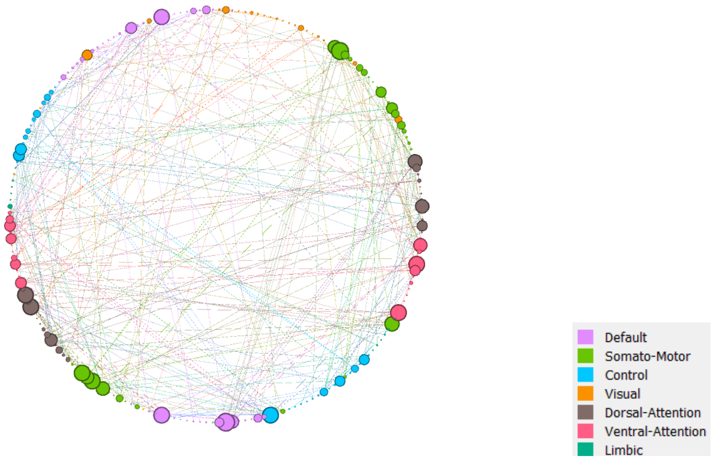

Figure 3.31: MK eigenvector connectivity graph.

MK EIGENVECTOR CENTRALITY		
Top 5	**Eigenvector**	**Functional Network**
RH Default Temp 4	1	Default
RH SomMot 2	0.961	Somato-Motor
RH SomMot 13	0.888	Somato-Motor
RH SomMot 15	0.888	Somato-Motor
LH DorsAttn Post 10	0.888	Dorsal-Attention

Table 3.19: MK connectivity eigenvector centrality.

Concerning the last kurtosis metric taken into consideration, the RK connectivity graph shows some similar results compared to the FA network. In particular, the presence of hubs belonging principally to the Default and Somato-Motor functional networks is shared by these two metrics, along with the poor degree score showed by Visual and Control areas. However, contrarily to FA degree connectivity graph, for RK there is a hub distribution mainly concentrated on the LH of the brain, as it can be clearly seen from the top 5 scoring hubs of the RK degree network. Being both FA and RK measures of white matter tract integrity, no inferences on the activation synchronization can be made, but they offer different insights to be integrated if a comprehensive view is desired.

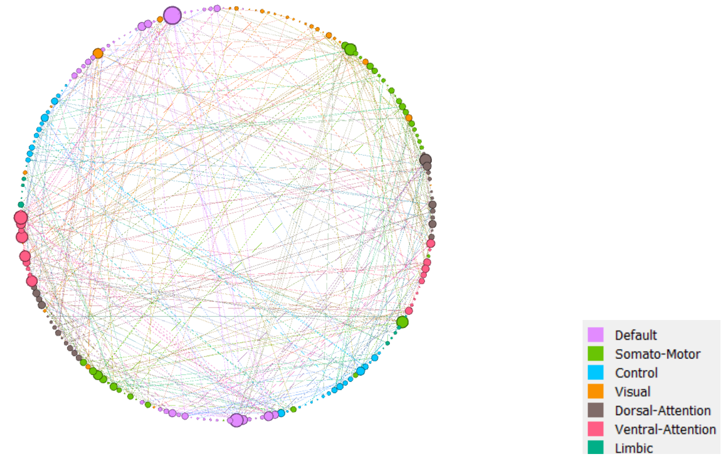

Figure 3.32: RK degree connectivity graph.

RK DEGREE CENTRALITY		
Top 5 Hubs	**Degree**	**Functional Network**
LH Default PFC 9	19	Default
LH SalVentAttn Med 2	14	Ventral-Attention
RH Default Temp 4	14	Default
LH SomMot 2	12	Somato-Motor
LH SalVentAttn FrOperIns 4	12	Ventral-Attention

Table 3.20: RK connectivity degree centrality.

Regarding the betweenness estimation extracted from the RK graph, it can be noticed a resemblance with the FA output results. In fact, also here there main bridge roles are played by Dorsal-,Ventral-Attention and Default functional networks nodes. On the other hand, in the top 5 betweenness scoring vertices, RK connectivity identifies the principal interconnection region in the Control network area, while for FA this node belong to the Dorsal-Attention functional zone. In addition, it is evident from the graphical representation that the Default network contributes significantly for the architecture interconnection.

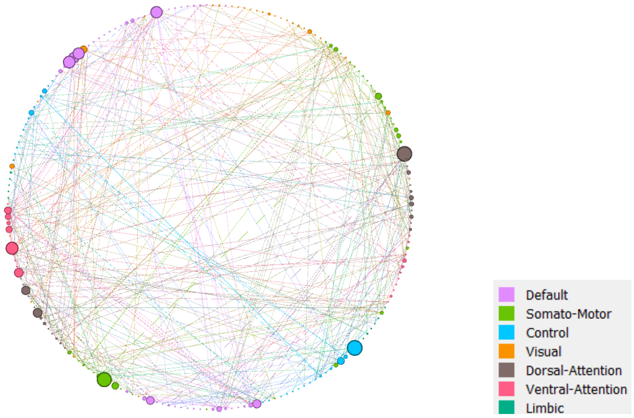

Figure 3.33: RK betweenness connectivity graph.

RK BETWEENNESS CENTRALITY		
Top 5	**Betweenness**	**Functional Network**
RH Cont Par 2	1351	Control
RH DorsAttn Post 2	1327	Dorsal-Attention
LH SomMot 10	1281	Somato-Motor
LH SalVentAttn FrOperIns 2 8	1079	Ventral-Attention
LH Default Temp 4	1051	Default

Table 3.21: RK connectivity betweenness centrality.

To conclude the network analysis of the RK connectivity graph, the eigenvector centrality measure was also computed. It is clear not only from the graphical representation, but also from the reported top 5 scoring nodes, that the most influent nodes belong almost exclusively to the Default and Somato-Motor functional networks. This behaviour is much different compared to the results obtained for FA, therefore it may be reasonable to assume that RK outputs could bring additional information to be integrated in order to have a satisfactory overview of the network connections, as for the FA and RK degree centrality measure.

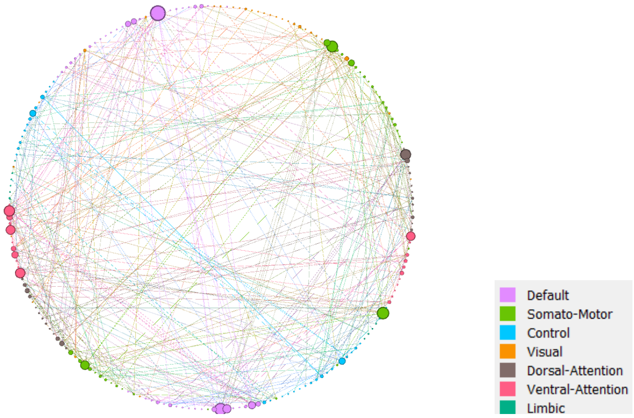

Figure 3.34: RK eigenvector connectivity graph.

RK EIGENVECTOR CENTRALITY		
Top 5	**Eigenvector**	**Functional Network**
LH Default PFC 9	1	Default
LH Default Temp 0.770	1051	Default
LH SomMot 2	0.761	Somato-Motor
RH SomMot 2	0.714	Somato-Motor
LH SalVentAttn Med 2	0.680	Ventral-Attention

Table 3.22: RK connectivity eigenvector centrality.

Finally, a particular insight is given by the combination of MD and MK connectivity graphs. In fact, by keeping only the connections identified by both MD and MK connectivity matrices, it is possible to obtain the combined network configuration. As for all the diffusion and diffusion kurtosis metrics, also in this context the degree, betweenness and eigenvector centrality measures. Starting from the degree centrality, the intragration of the diffusion connectivity graphs returns the hypothesis of synchronized activation mainly of the Dorsal-Attention, Default and Somato-Motor functional networks. This is in line with both of the output results found for both MD and MK, leading to the conclusion that these areas could operate simultaneously, given that a similar diffusion pattern could mean a high activation correlation.

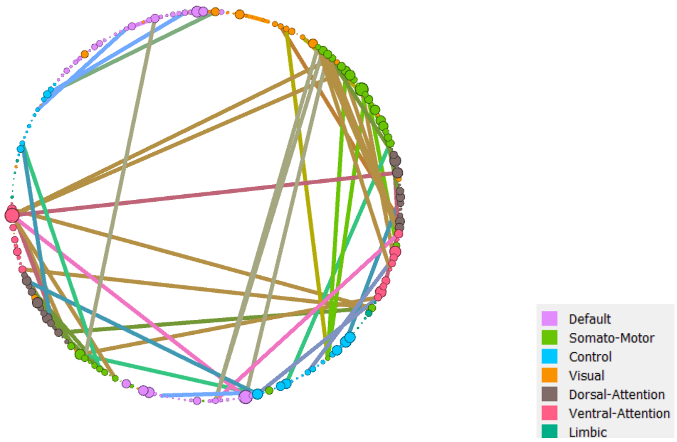

Figure 3.35: MD and MK degree connectivity graph.

MD and MK DEGREE CENTRALITY		
Top 5 Hubs	**Degree**	**Functional Network**
LH SalVentAttn Med 1	43	Dorsal-Attention
RH Default Par 2	40	Default
RH SomMot 10	39	Somato-Motor
RH DorsAttn Post 3	33	Dorsal-Attention
RH SalVentAttn TempOccPar	33	Ventral-Attention

Table 3.23: MD and MK connectivity degree centrality.

Moving to the betweenness centrality measure combination, this result to be a bit different compared to the merged results of MD and MK singularly. In fact, the Visual network, which was a key bridge area for both MD and MK connectivity graphs, does not contribute so much in the information signal interchange in the combined network configuration. However, the prevalence of the Dorsal-Attention and Default and functional networks as main activation information exchange areas, suggests that these could be the more important linking brain regions for correlated triggering.

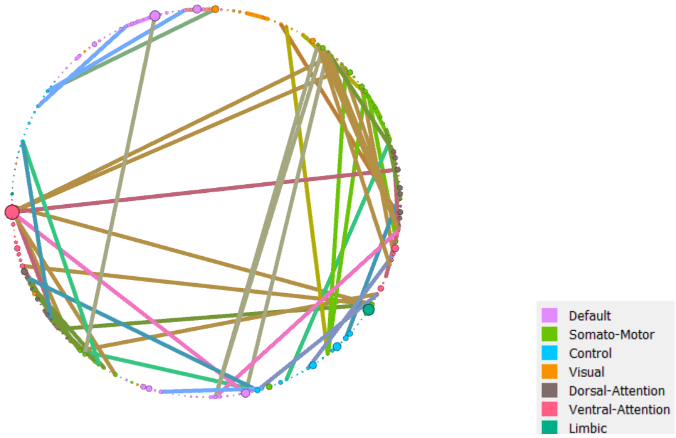

Figure 3.36: MD and MK betweenness connectivity graph.

MD and MK BETWEENNESS CENTRALITY		
Top 5	**Betweenness**	**Functional Network**
LH SalVentAttn Med 1	1301	Dorsal-Attention
RH Limbic OFC 2	996	Limbic
LH Default PFC 9	899	Default
RH Default Par 2	726	Default
LH Default pCunPCC 3	696	Default

Table 3.24: MD and MK connectivity betweenness centrality.

Finally, the combined eigenvector results show almost a perfect intersection of the MD and MK findings combination. In fact, if in MK the main influent brain network is the Somato-Motor, along with the Default area, and in MD there is also the important presence of the Ventral-Attention region, here the integration of this different results leads to the outcome of identifying as main activation influence regions both the Somato-Motor and Default functional networks, followed by the Ventral and Dorsal Attention areas. These findings may suggest not only that the above mentioned regions could influence the triggering chain among themselves and also the other functional zones of the brain, but also that the nodes belonging to these functional networks have the highest transitive activation control on the other brain areas.

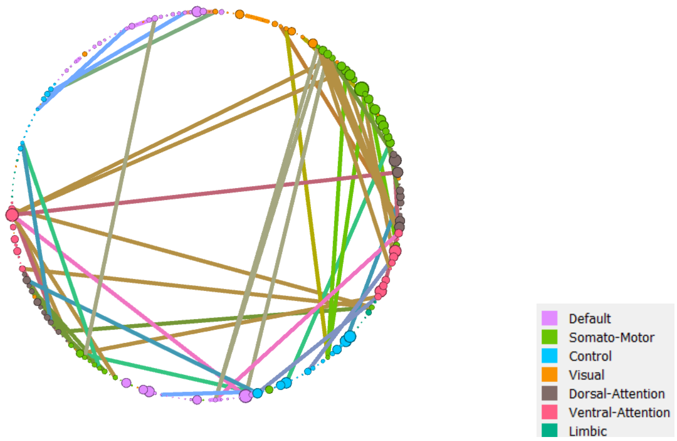

Figure 3.37: MD and MK eigenvector connectivity graph.

MD and MK EIGENVECTOR CENTRALITY		
Top 5	**Eigenvector**	**Functional Network**
RH SomMot 10	1	Somato-Motor
RH Default Par 2	0.902	Default
LH SalVentAttn Med 1	0.874	Ventral-Attention
RH DorsAttn Post 3	0.834	Dorsal-Attention
RH SalVentAttn TempOccPar 3	0.808	Ventral-Attention

Table 3.25: MD and MK connectivity eigenvector centrality.

Chapter 4

Discussion

4.1 Sensibility Analysis

Concerning the first subject under investigation, the boxplots of the diffusion metrics, both revealed a clear distinction of Tumor Non-enhancing region from the regions of Tumor Enhancing and Oedema areas. More specifically, FA and MD, were not able to separate the Tumor Enhancing and Oedema regions, both in terms of difference in values and distribution. On the other hand, MK and RK boxplots are very similar to each other, showing how the value distribution of the Tumor Oedema area is much different compared to the Enhancing and Non-enhancing sections. Moving to the second individual, MD and FA boxplots are more capable of distinguishing the three tumoral regions, even if with a marginal variation from the precedent case. The same happens when evaluating the kurtosis metrics, for which the boxplots highlight not only the similarity of classification of MK and RK, but also the high dissimilarity of the distribution of the values in the three tissue involved. For the third patient, MD boxplots are not able to provide a significant separation among the different tissues and only carry information about the value distribution. Contrarily, FA seems to be a more valuable measure to distinguish the diverse tumoral tissue area. MK furnish an acceptable differentiation of Tumor Non-enhancing region compared to Enhancing and Oedema areas, while RK allows for a complete distinction of all diseased tissue taken into consideration, resulting in the most reliable sensibility index. To conclude the discussion of the sensibility analysis of the subjects with 3 different tumor tissues, only MD and FA can provide an acceptable differentiation performance. MK and RK instead cannot separate the tissue types in an acceptable manner, but they give important information about the value distribution in the diseased regions. The other remaining results regard the sensibility on all the four tumoral tissue types. In the first case, diffusion metrics can provide a valuable diversification and the kurtosis measures exhibit more or less the same trend. In particular, FA oxplots produce an even more accurate tumoral tissue differentiation, resulting to be a reliable sensibility index, while

MK shows a good distinction property among Tumor Necrosis, Enhancing and Non-enhancing regions, while presenting only a subtle contrast between Tumor Necrosis and Oedema area. Concerning the second complete individual, the kurtosis metrics showed a higher sensibility compared to the diffusion indices. In fact, MK and RK, which show more or less the same value and distribution of the different diseased tissues, are able to provide a reliable differentiation and may be used for the identification of the tumor region-specific tissue. In the following subject, the metrics sensibility quite resembles the situation seen for the previous individual. In fact, the only valuable differentiation showed by MD boxplots is the one of the Tumor Non-enhancing region from the other three tumor areas. Kurtosis metrics instead, sis metrics exhibit a similar classification between each other. Precisely, both MK and RK boxplots reveal significant differences in the Tumor Non-enhancing area compared to the remaining three tissues. A similar situation is displyed by the sensibility assessment for the following individual. In fact, MD and FA boxplots are able to show a significant distinction only for the Tumor Non-enhancing zone. Contrarily, MK and RK boxplots identify a valuable separation between the two couples of tumoral tissue composed byTumor Necrosis and Enhancing, and Tumor Non-enhancing and Oedema. In this case, RK results to be slightly more sensible compared to MK. For the second-last investigated patient diffusion metrics are to be considered more reliable compared to the kurtosis ones. In fact, both MD and FA can distinguish the Tumor Enhancing and Non-enhancing regions from the rest of the tumoral tissue. Concering the kurtosis metrics instead, MK and RK are both only able to separate the Tumor Non-enhancing area from the other ones, and only slight differences can be noted among the Tumor Necrosis, Enhancing and Oedema zones. The last included subject shows a similar differentiation trend compared to the previous individual.

4.2 Network Analysis

Starting from the raw connectivity matrices, both the diffusion and kurtosis microparameters show evident clustered configuration that reveals the different brain functional networks. In particular, this kind of pattern is more observable for MD and MK matrices that can well capture the diffusion dynamics in the gray matter cortical regions. FA and RK, being metrics of white matter integrity estimation, are less able to identify the brain functional block structures, even if they are still notable. In addition, the p-value correlation corrected network reveals some interesting outcomes. Starting from FA degree measure, it shows how the most important hubs are placed in the right hemisphere of the brain functional organization. In particular, they belong to the Attention, Default and Somato-Motor networks, which are to be considered the most triggered areas. Regarding FA betweenness centrality results, these are found to be very similar to the previous mentioned case. On the other hand, much different is the network configuration concerning the eigenvector centrality of the FA connectivity graph. In fact, here almost all functional networks are included in describing the influence of brain regions over others, excluding only the Limbic and Visual functional areas. Moving to the MD connectivity analysis results, here it is possible to make inference regarding the activation synchronization and influence, along with activation information signal transfer, given by degree, eigenvector and betweenness centrality measures. Starting from the hubs identification, it is clear that the major hub nodes belong to the Attention networks, both Dorsal and Ventral, followed by Somato-Motor and Default networks. Given this situation, it may be probable that in glioma patients the Attention, Default and Somato-Motor functional networks activation could by synchronized. Moving to the betwennees centrality measure extracted from the MD connectivity graph, it is evident from the graphical representation that the main bridge roles of the network are played by brain regions member of Ventral-Attention, Somato-Motor and Visual functional networks. In this context, it is also noteworthy to mention the Default and Dorsal-Attention areas. Concerning the eigenvector estimated scores, it has to be highlighted the fact that the most influent brain regions are mainly associated to Somato-Motor and Default functional networks. These findings may signify that the above mentioned brain regions could be the most important in terms of activation influence, causing the partial triggering also of the connected functional areas. In addition, a minor contribution is given by the Ventral-Attention and Control networks. The second part of the network analysis discussion regards the kurtosis metrics connectivity graphs. Given that the MK metric is suitable also for model the diffusion dynamics in GM regions, it has to be highlighted that MK connectivity results may give the possibility to hypothesize functional activation triggering patterns, as said for MD findings. Starting from MK degree centrality outcomes, the most important nodes correspond with the same functional networks found in the MD graph, specifically the Dorsal and Ventral-Attention networks, along with Default and Somato-Motor functional areas. However, for MK the top 5 scoring hubs principally belong to the brain left hemispher (LH), showing how the MK metric provides an integration of information concerning the brain network synchronized functional configuration. Also for the betwenness measure MD shares a similar top 5 scoring regions, suggesting that the Dorsal-Attention, Somato-Motor and Visual areas may be covering the most important roles for the activation information signal transfer. Concerning the last centrality measure of MK connectivity graph, the eigenvector scores show that there is a different distribution pattern compared to the one of MD. In fact, for MK there is a completely dominance of the Somato-Motor regions over the others, in term of activation influence. Default and Somato-Motor functional networks may be the mainly activation regulators of the brain functional activity, followed by the Attention networks, both Dorsal and Ventral, and the Control areas. Taking into consideration the last kurtosis metric connectivity graph, RK in general shows some similar results compared to the ones obtained for FA. In fact, regarding the degree centrality measures, the top 5 scoring hubs belong principally to the Default and Somato-Motor functional networks, along with the poor degree contribution showed by Visual and Control areas. However, contrarily to FA degree connectivity graph, for RK there is a hub distribution mainly concentrated on the LH of the brain. Unfortunately, as for FA, also in this context no inferences on the activation synchronization can be made, but they offer different insights that need to be taken into consideration for a broader analysis. Also in the betweenness estimation of RK connectivity graph a resemblance with FA results can be noticed. In fact, the main bridge roles are played by Dorsal-,Ventral-Attention and Default functional networks nodes. However, RK connectivity identifies the principal interconnection region in the Control network area, while for FA this node belong to the Dorsal-Attention functional zone. For both FA and RK, the Default network contributes significantly for the architecture interconnection. From the eigenvector centrality measure, it is evident that the most influent nodes belong almost exclusively to the Default and Somato-Motor functional networks. This pattern is much different compared to the results obtained for FA, therefore it may be reasonable to assume that RK outputs could bring additional information to the overall diffusion microstructural connectivity analysis. Finally, peculiar insights coulb be given by the network organization built from the combination of both MD and MK connectivity matrices. Concerning the degree centrality measure, the results suggest that the mainly synchronized regions correspond to the Dorsal-Attention, Default and Somato-Motor functional networks. This is in line with both of the output results found for both MD and MK, leading to the conclusion that these areas could operate simultaneously. Moving to the betweenness centrality measure combination, the prevalence of the Dorsal-Attention and Default and functional networks as main activation information exchange areas, suggests that these could be the more important linking brain regions for correlated triggering. However, he Visual network, which was a key bridge area for both MD and MK connectivity graphs, does not contribute so much in the information signal interchange in the combined network configuration. Finally, the eigenvector estimation returns the integration of the different results from MD and MK, leading to the outcome of identifying as main activation influence regions both the Somato-Motor and Default functional networks, followed by the Ventral and Dorsal Attention areas. These findings may indicate that the nodes belonging to the functional networks just mentioned have the highest transitive activation control on the other brain areas.

Chapter 5

Conclusions

This thesis proposes the innovative idea of microparameters connectivity investigation. This means that, thanks to the exploitation of a new neural network optimization-based fitting model, it was possible to evaluate the diffusion microparameters pattern, of a pool of selected subjects affected by de novo glioma, through graph theory methodologies.

By virtue of diffusion MRI, which is one of the most valuable tools for explore the human brain structural composition, the DKI reconstruction model was applied in order to provide a broader description of the brain microstructural organization, by the assessment of both diffusion and diffusion kurtosis metrics. In particular, the optimized version of this model allows to compute reliable estimations thanks both to the regularization and stabilization terms that contribute to the final parameters computation.

Then, knowing the potential application of DKI in the context of gliomas, a tumor-specific sensibility analysis was carried out to test the accuracy capability of the implemented model. To this end, both diffusion and diffusion kurtosis indices were extracted and evaluated for the different types of the tumor tissue.

Certainly the results of this sensibility study were biased not only by the different sizes of the tumor tissue types, but also by the diverse pathological situation of the included individuals, but it revealed some interesting findings that may inspire the future use of this kind of methodology to furnish more precise diagnostic and prognostic assessments.

In addition, the computed indices maps were utilized to build the diffusion microstructural connectivity matrices, which are a new investigation method to be correlated with the human brain functional activity. In fact, by capturing the diffusion pattern of the cortical brain regions and implementing a multi-subject correlation study, it is possible to evaluate the brain functional activation from a network prospective, especially for the diffusion and kurtosis metrics that can model the water molecules displacement dynamics in grey matter areas.

Therefore, the brain diffusion microstructural network representation was used to extract meaningful centrality measures to be associated mainly with synchronized and influenced functional triggering. Unfortunately, this project does not analyze the correlation between this network model procedure and functional MRI data, but the obtained results are interpretable enough to make reasonable inferences.

To conclude, future brain disease investigations should include the diffusion MRI data in order to have additional and valuable information regarding the dynamics of the pathology taken into consideration. In particular, both structural and region-specific diffusion microstuctural connectivity, along with network analysis, are emerging methodologies which are increasingly contributing to help neurologists and neuroradiologists in identifying not only patient-designed therapies, but also suitable prevention strategies.

Bibliography

[1] J. A. Schwartzbaum, J. L. Fisher, K. D. Aldape, and M. Wrensch, "Epidemiology and molecular pathology of glioma," *Nature clinical practice Neurology*, vol. 2, no. 9, pp. 494–503, 2006.

[2] M. Weller, W. Wick, K. Aldape, M. Brada, M. Berger, S. M. Pfister, R. Nishikawa, M. Rosenthal, P. Y. Wen, R. Stupp, *et al.*, "Glioma," *Nature reviews Disease primers*, vol. 1, no. 1, pp. 1–18, 2015.

[3] A. Perry and P. Wesseling, "Histologic classification of gliomas," *Handbook of clinical neurology*, vol. 134, pp. 71–95, 2016.

[4] W. B. Pope and G. Brandal, "Conventional and advanced magnetic resonance imaging in patients with high-grade glioma," *The quarterly journal of nuclear medicine and molecular imaging: official publication of the Italian Association of Nuclear Medicine (AIMN)[and] the International Association of Radiopharmacology (IAR),[and] Section of the Society of...*, vol. 62, no. 3, p. 239, 2018.

[5] K. O. Almansory and F. Fraioli, "Combined pet/mri in brain glioma imaging," *British Journal of Hospital Medicine*, vol. 80, no. 7, pp. 380–386, 2019.

[6] W. Taal, J. E. Bromberg, and M. J. van den Bent, "Chemotherapy in glioma," *CNS oncology*, vol. 4, no. 3, pp. 179–192, 2015.

[7] D. N. Louis, A. Perry, P. Wesseling, D. J. Brat, I. A. Cree, D. Figarella-Branger, C. Hawkins, H. Ng, S. M. Pfister, G. Reifenberger, *et al.*, "The 2021 who classification of tumors of the central nervous system: a summary," *Neuro-oncology*, vol. 23, no. 8, pp. 1231–1251, 2021.

[8] D. N. Louis, E. C. Holland, and J. G. Cairncross, "Glioma classification: a molecular reappraisal," *The American journal of pathology*, vol. 159, no. 3, p. 779, 2001.

[9] P. Y. Wen and D. A. Reardon, "Progress in glioma diagnosis, classification and treatment," *Nature Reviews Neurology*, vol. 12, no. 2, pp. 69–70, 2016.

[10] A. Claes, A. J. Idema, and P. Wesseling, "Diffuse glioma growth: a guerilla war," *Acta neuropathologica*, vol. 114, no. 5, pp. 443–458, 2007.

[11] N. A. O. Bush, S. M. Chang, and M. S. Berger, "Current and future strategies for treatment of glioma," *Neurosurgical review*, vol. 40, no. 1, pp. 1–14, 2017.

[12] R. D. Tien, G. Felsberg, H. Friedman, M. Brown, and J. MacFall, "Mr imaging of high-grade cerebral gliomas: value of diffusion-weighted echo-planar pulse sequences.," *AJR. American journal of roentgenology*, vol. 162, no. 3, pp. 671–677, 1994.

[13] T. Sugahara, Y. Korogi, M. Kochi, I. Ikushima, Y. Shigematu, T. Hirai, T. Okuda, L. Liang, Y. Ge, Y. Komohara, *et al.*, "Usefulness of diffusion-weighted mri with echo-planar technique in the evaluation of cellularity in gliomas," *Journal of Magnetic Resonance Imaging: An Official Journal of the International Society for Magnetic Resonance in Medicine*, vol. 9, no. 1, pp. 53–60, 1999.

[14] K. M. Schmainda, "Diffusion-weighted mri as a biomarker for treatment response in glioma," *CNS oncology*, vol. 1, no. 2, pp. 169–180, 2012.

[15] C. Geer, J. Simonds, A. Anvery, M. Chen, J. Burdette, M. Zapadka, T. Ellis, S. Tatter, G. Lesser, M. Chan, *et al.*, "Does mr perfusion imaging impact management decisions for patients with brain tumors? a prospective study," *American journal of neuroradiology*, vol. 33, no. 3, pp. 556–562, 2012.

[16] Y. Bai, Y. Lin, J. Tian, D. Shi, J. Cheng, E. M. Haacke, X. Hong, B. Ma, J. Zhou, and M. Wang, "Grading of gliomas by using monoexponential, biexponential, and stretched exponential diffusion-weighted mr imaging and diffusion kurtosis mr imaging," *Radiology*, vol. 278, no. 2, pp. 496–504, 2016.

[17] G. A. Gihr, D. Horvath-Rizea, E. Hekeler, O. Ganslandt, H. Henkes, K.-T. Hoffmann, C. Scherlach, and S. Schob, "Histogram analysis of diffusion weighted imaging in low-grade gliomas: in vivo characterization of tumor architecture and corresponding neuropathology," *Frontiers in Oncology*, vol. 10, p. 206, 2020.

[18] G. Gihr, D. Horvath-Rizea, E. Hekeler, O. Ganslandt, H. Henkes, K.-T. Hoffmann, C. Scherlach, and S. Schob, "Diffusion weighted imaging in high-grade gliomas: A histogram-based analysis of apparent diffusion coefficient profile," *Plos one*, vol. 16, no. 4, p. e0249878, 2021.

[19] J. Cluceru, Y. Interian, J. J. Phillips, A. M. Molinaro, T. L. Luks, P. Alcaide-Leon, M. P. Olson, D. Nair, M. LaFontaine, A. Shai, *et al.*, "Improving the noninvasive classification of glioma genetic subtype with deep learning and diffusion-weighted imaging," *Neuro-oncology*, vol. 24, no. 4, pp. 639–652, 2022.

[20] J. Jefferys and A. Cooper, “Brain basics,” *The Human Brain and Its Disorders*, 2007.

[21] V. P. Grover, J. M. Tognarelli, M. M. Crossey, I. J. Cox, S. D. Taylor-Robinson, and M. J. McPhail, “Magnetic resonance imaging: principles and techniques: lessons for clinicians,” *Journal of clinical and experimental hepatology*, vol. 5, no. 3, pp. 246–255, 2015.

[22] D. Le Bihan, J.-F. Mangin, C. Poupon, C. A. Clark, S. Pappata, N. Molko, and H. Chabriat, “Diffusion tensor imaging: concepts and applications,” *Journal of Magnetic Resonance Imaging: An Official Journal of the International Society for Magnetic Resonance in Medicine*, vol. 13, no. 4, pp. 534–546, 2001.

[23] E. O. Stejskal and J. E. Tanner, “Spin diffusion measurements: spin echoes in the presence of a time-dependent field gradient,” *The journal of chemical physics*, vol. 42, no. 1, pp. 288–292, 1965.

[24] L. J. O’Donnell and C.-F. Westin, “An introduction to diffusion tensor image analysis,” *Neurosurgery Clinics of North America*, vol. 22, no. 2, pp. 185–196, 2011. Functional Imaging.

[25] E. X. Wu and M. M. Cheung, “Mr diffusion kurtosis imaging for neural tissue characterization,” *NMR in Biomedicine*, vol. 23, no. 7, pp. 836–848, 2010.

[26] J. H. Jensen, J. A. Helpern, A. Ramani, H. Lu, and K. Kaczynski, “Diffusional kurtosis imaging: the quantification of non-gaussian water diffusion by means of magnetic resonance imaging,” *Magnetic Resonance in Medicine: An Official Journal of the International Society for Magnetic Resonance in Medicine*, vol. 53, no. 6, pp. 1432–1440, 2005.

[27] A. J. Steven, J. Zhuo, and E. R. Melhem, “Diffusion kurtosis imaging: an emerging technique for evaluating the microstructural environment of the brain,” *American journal of roentgenology*, vol. 202, no. 1, pp. W26–W33, 2014.

[28] R. Jiang, J. Jiang, L. Zhao, J. Zhang, S. Zhang, Y. Yao, S. Yang, J. Shi, N. Shen, C. Su, *et al.*, “Diffusion kurtosis imaging can efficiently assess the glioma grade and cellular proliferation,” *Oncotarget*, vol. 6, no. 39, p. 42380, 2015.

[29] A. Tonoyan, I. Pronin, D. Pitshelauri, L. Shishkina, L. Fadeeva, E. Pogosbekyan, N. Zakharova, E. Shults, N. Khachanova, V. Kornienko, *et al.*, “A correlation between diffusion kurtosis imaging and the proliferative activity of brain glioma,” *Zh Vopr Neirokhir Im NN Burdenko*, vol. 79, no. 6, pp. 5–14, 2015.

[30] F. Li, W. Shi, D. Wang, Y. Xu, H. Li, J. He, and Q. Zeng, "Evaluation of histopathological changes in the microstructure at the center and periphery of glioma tumors using diffusional kurtosis imaging," *Clinical Neurology and Neurosurgery*, vol. 151, pp. 120–127, 2016.

[31] J.-M. Hempel, S. Bisdas, J. Schittenhelm, C. Brendle, B. Bender, H. Wassmann, M. Skardelly, G. Tabatabai, S. C. Vega, U. Ernemann, *et al.*, "In vivo molecular profiling of human glioma using diffusion kurtosis imaging," *Journal of neuro-oncology*, vol. 131, no. 1, pp. 93–101, 2017.

[32] X.-f. Wu, X. Liang, X.-c. Wang, J.-b. Qin, L. Zhang, Y. Tan, and H. Zhang, "Differentiating high-grade glioma recurrence from pseudoprogression: Comparing diffusion kurtosis imaging and diffusion tensor imaging," *European Journal of Radiology*, vol. 135, p. 109445, 2021.

[33] Y. Li, M. M. Kim, D. R. Wahl, T. S. Lawrence, H. Parmar, and Y. Cao, "Survival prediction analysis in glioblastoma with diffusion kurtosis imaging," *Frontiers in Oncology*, vol. 11, 2021.

[34] J. Qiu, K. Deng, P. Wang, C. Chen, Y. Luo, S. Yuan, and J. Wen, "Application of diffusion kurtosis imaging to the study of edema in solid and peritumoral areas of glioma," *Magnetic resonance imaging*, vol. 86, pp. 10–16, 2022.

[35] M. Van Steen, "Graph theory and complex networks," *An introduction*, vol. 144, 2010.

[36] F. A. Rodrigues, "Network centrality: an introduction," in *A mathematical modeling approach from nonlinear dynamics to complex systems*, pp. 177–196, Springer, 2019.

[37] F. V. Farahani, W. Karwowski, and N. R. Lighthall, "Application of graph theory for identifying connectivity patterns in human brain networks: a systematic review," *frontiers in Neuroscience*, vol. 13, p. 585, 2019.

[38] O. Sporns, D. R. Chialvo, M. Kaiser, and C. C. Hilgetag, "Complex networks: small-world and scale-free architectures," *Trends in Cognitive Sciences*, vol. 9, no. 8, pp. 418–425, 2004.

[39] O. Sporns, G. Tononi, and R. Kötter, "The human connectome: a structural description of the human brain," *PLoS computational biology*, vol. 1, no. 4, p. e42, 2005.

[40] M. Rubinov and O. Sporns, "Complex network measures of brain connectivity: uses and interpretations," *Neuroimage*, vol. 52, no. 3, pp. 1059–1069, 2010.

[41] O. Sporns, "Network attributes for segregation and integration in the human brain," *Current opinion in neurobiology*, vol. 23, no. 2, pp. 162–171, 2013.

[42] M. P. Van Den Heuvel and O. Sporns, “Rich-club organization of the human connectome,” *Journal of Neuroscience*, vol. 31, no. 44, pp. 15775–15786, 2011.

[43] O. Sporns, “Graph theory methods: applications in brain networks,” *Dialogues in clinical neuroscience*, 2022.

[44] D. Papo, J. M. Buldú, S. Boccaletti, and E. T. Bullmore, “Complex network theory and the brain,” 2014.

[45] E. Silvestri, U. Villani, M. Moretto, M. Colpo, A. Salvalaggio, M. Anglani, M. Castellaro, S. Facchini, E. Monai, D. D’Avella, *et al.*, “Assessment of structural disconnections in gliomas: comparison of indirect and direct approaches,” *Brain Structure and Function*, pp. 1–12, 2022.

[46] J. Veraart, W. Van Hecke, and J. Sijbers, “Constrained maximum likelihood estimation of the diffusion kurtosis tensor using a rician noise model,” *Magnetic resonance in medicine*, vol. 66, no. 3, pp. 678–686, 2011.

[47] R. N. Henriques, S. N. Jespersen, D. K. Jones, and J. Veraart, “Toward more robust and reproducible diffusion kurtosis imaging,” *Magnetic Resonance in Medicine*, vol. 86, no. 3, pp. 1600–1613, 2021.

[48] L. Kerkelä, K. Seunarine, R. N. Henriques, J. D. Clayden, and C. A. Clark, “Improved reproducibility of diffusion kurtosis imaging using regularized non-linear optimization informed by artificial neural networks,” *arXiv preprint arXiv:2203.07327*, 2022.

[49] O. Eidel, S. Burth, J.-O. Neumann, P. J. Kieslich, F. Sahm, C. Jungk, P. Kickingereder, S. Bickelhaupt, S. Mundiyanapurath, P. Baumer, *et al.*, “Tumor infiltration in enhancing and non-enhancing parts of glioblastoma: a correlation with histopathology,” *PloS one*, vol. 12, no. 1, p. e0169292, 2017.

[50] A. Lasocki and F. Gaillard, “Non-contrast-enhancing tumor: a new frontier in glioblastoma research,” *American Journal of Neuroradiology*, vol. 40, no. 5, pp. 758–765, 2019.

[51] S. M. Nehring, P. Tadi, and S. Tenny, “Cerebral edema,” in *StatPearls [Internet]*, StatPearls Publishing, 2021.

[52] S. Bakas, M. Reyes, A. Jakab, S. Bauer, M. Rempfler, A. Crimi, R. T. Shinohara, C. Berger, S. M. Ha, M. Rozycki, *et al.*, “Identifying the best machine learning algorithms for brain tumor segmentation, progression assessment, and overall survival prediction in the brats challenge,” *arXiv preprint arXiv:1811.02629*, 2018.

[53] A. Schaefer, R. Kong, E. M. Gordon, T. O. Laumann, X.-N. Zuo, A. J. Holmes, S. B. Eickhoff, and B. T. Yeo, “Local-global parcellation of the human cerebral cortex from intrinsic functional connectivity mri,” *Cerebral cortex*, vol. 28, no. 9, pp. 3095–3114, 2018.